Surface motion analysis for the natural ankle and for Total Ankle Replacements with different articular surface geometries.

A Thesis

Submitted to the Faculty

of

Drexel University

by

Rewati Pradeep Kulkarni

in partial fulfillment of the

requirements for the degree

of

Master of Science in Mechanical Engineering

September 2016

DEDICATIONS

I dedicate this thesis to my parents. They have given me unconditional support through all my struggles, the confidence to take chances, and the encouragement to pursue all my goals in life.

ACKNOWLEDGMENTS

TABLE OF CONTENTS

LIST OF TABLES

LIST OF FIGURES

ABSTRACT

Surface motion analysis for the natural ankle and for Total Ankle Replacements with different articular surface geometries.
Rewati Pradeep Kulkarni
Sorin Siegler, Ph.D.

The increasing success and establishment of arthroplasty procedures of the knee and hip over the years, has been reason enough for the want to create a functional Total Ankle Replacement, in an attempt to phase out ankle arthodesis. The implant models such as those developed by Inman and Buechel-Pappas were critical to this process gaining momentum. Most recently, the work of Siegler et al. proposed a new patient specific and anatomically accurate model of a TAR, which also attempts to reproduce the implant models with ligament stability, mechanical alignment, and joint kinematics.

This study focusses on one of the aspects of joint kinematics of the ankle complex, namely, the surface to surface interaction of the bones and its analysis during the various types of motion, by means of distance mapping.

During the physical experimentation, the individual bones of the ankle joint complex are fitted with fiduciary markers, which enables the recording of position data at predefined time steps and applied torque. This is done for the different *neutral* positions of the ankle, as well as the different types of motion of the ankle joint, namely, dorsi-plantar flexion, inversion-eversion, and internal-external rotation.

These distance maps are gradient patterns on the articulating surfaces taken in pairs, which provide us with information regarding the displacement of the concerned bones at every time step, for a specific motion type. By studying these maps, we hope to achieve a more definitive analysis of the surface interaction of the bones whilst fit with a TAR model, thus helping us achieve an implant design with the best morphological replications.

CHAPTER 1: INTRODUCTION

With the onset of increasingly successful routine surgeries of the hip and knee joints back in the 1970s,

many surgeons were of the belief that the replacement of the ankle would be just as easy and would yield

desirable results, similar to the excellent rate of success as observed with total hips and knees. However,

the complex biomechanics of the human ankle joint proved otherwise; early attempts at a total ankle

arthroplasty, which seemed to give successful results in the short term, in fact deteriorated quite rapidly.

The single working solution for end-stage osteoarthritis still remained an ankle arthrodesis, which again

addressed the problem only partially, due to the post-operative complications and limited mobility of the

joint.

Early TAR designs assumed that the ankle joint contained only one degree of freedom akin to a hinge

joint. This is the assumption that lead to the development and subsequent failure of ankle joints which

were oversimplified in their design. Over time, studies of the ankle's biomechanics yielded that the ankle

does not have a fixed axis of rotation, which lead to the development of implants with the ability to slide,

translate, and rotate.

Current TAR's are based off of a number of designs, some of the chief ones being: (1) the findings of

Inman, which describe the talar dome as a frustum of a symmetrical cone that apexes medially and

contains a saddle, (2) the cylindrical talar implant similar to the one designed by Beuchel-Pappas, and (3) a

symmetrical conic model that apexes laterally. In addition, the studies done by Siegler show that the talar

dome can be approximated as a frustum of a skewed cone that apexes laterally *and* contains a saddle.

Given the variety of TAR models, and the minute differences between them, it is imperative to determine

a methodology to evaluate these models. The most relevant method is via analysis of the kinematic

behavior of each model type. While an extensive kinematic study involves multiple considerations such as

ligament fixations, flexibility studies, and coupling characteristics, the primary goal of this study was to

focus on one of the aspects of joint kinematics of the ankle complex, namely, the surface to surface

interaction of the bones by distance mapping, during the three types of motion of the ankle: Dorsi flexion/Plantar flexion, Internal rotation/External rotation, and Inversion/Eversion.

Methods of evaluation of TAR

Kinematic studies on current TAR models have been performed largely by means of gait analysis, which involves the evaluation of the motion of the foot and ankle together. Modern gait analysis uses 3-dimensional optical tracking methods in which tracking markers are placed on the skin over palpable landmarks [1] which are activated upon motion, thus allowing the observer to electronically collect the kinematic data over a global coordinate system. The study conducted by Brodsky et al. performed 3-dimensional gait analysis on patients affected by osteoarthritis, and fitted with the Scandinavian Total Ankle Replacement (STAR) model. Kinematic data, which consisted of limb trajectories and joint angles [1] was collected using a 12-camera Vicon motion capture system [2] and was used to collect velocity data during gait, both pre-operatively and post-operatively. The study yielded that although there was a significant increase in gait velocity post-operatively, the peak ankle power dwindled over the course of three years, and thus called for a more effective study of range of motion with a TAR.

Another study performed by Iwamoto et al. focused on the in-vivo kinematics of three-component mobile-bearing Total Ankle Replacement in a rheumatoid ankle with talocalcaneal arthrodesis and spontaneous talocalcaneal fusion [3]. The study was performed on patients with severe rheumatoid arthritis whose talocalcaneal joints had naturally fused due to degeneration. Fluoroscopic images were obtained while each patient was walking with full weight bearing on the implanted ankle. Thereafter tibio–talar motion was analyzed by 2D/3D registration technique. The team concluded that the mobility of mobile-bearing TAR with talocalcaneal fusion was small during stance, but that the range of motion was still preserved.

A more relevant study conducted in recent times that by Hintermann et al., looked at the kinematic changes in talar movement after fusion and a TAR procedure. The team studied talar rotation and talar

shift during Dorsi flexion/Plantar flexion with respect to the tibia in the normal, fused, and prosthetically replaced ankle, using a 6-df device and a four-camera high-speed video system, to measure the range of motion (ROM) cadaveric leg specimens. Segmental

Motion, rotation, and medial-lateral shift of the marked bones of the foot and shank were measured dynamically. The movement data was collected at 5 second intervals, and the overall range of motion was from Dorsi to plantar flexion. The results yielded restricted (~ 80% decrease) talar motion in the ankle mortise for a two-component (AGILITY^{TM}) implant, and a larger range of talar motion for a three component implant (HINTEGRA^{TM}, S.T.A.R^{TM}). The team concluded that a successful prosthetic design for the ankle should consist of *three* components that are shaped as anatomically as possible to provide a normal range of motion [4].

However, the lack of surface mapping studies on two-component implant kinematics is evident from the fact that not much has been done as far as the measurement of actual displacement of the articulating surfaces is concerned. All the aforementioned studies deal with important aspects of post-surgical implant analysis, but the study of surface-to-surface displacement is crucial to implant kinematics, as a means of comparing the exact movements of the natural ankle to that of the implant-fit ankle. This is an important step in analyzing how far the implant is able to replicate the parameters of the natural ankle, such as motion combination, directional displacement, and tightness of fit throughout the ROM.

Primary goal and specific aims

The chief purpose of this study is to develop a standardized procedural method to evaluate the kinematic behavior of TAR through analysis of the articulating surfaces. In order to accomplish this goal, the following specific aims were outlined for the study:

1. Measure the morphological features of the 3-D renderings of the talus, tibia, and calcaneus.

2. Create the different implant models with the appropriate surface designs based on the morphological measurements done previously.

3. Fix the implants onto the bones, associate the fiduciary markers with each bone based on the insertion points as observed from the MRI scans, and organize the experimental position data to isolate the required points from the loading/unloading cycle.

4. Use this point position data to align the bones at every time step, and eventually perform a surface-to-surface 3-dimensional displacement analysis to obtain distance maps throughout the range of motion specified.

CHAPTER 2: BACKGROUND

Skeletal anatomy of the Ankle

The ankle complex is a combination of two major joints, namely, the talocrural and subtalar joints. The talocrural joint, or as is commonly known, the ankle joint, is the articulation between the distal ends of the tibia and fibula, with the proximal ends of the talus. The trochlear surface of the talus, i.e., the talar dome, articulates within the tibial plateau, which forms the ankle mortise. This is why the talocrural joint is sometimes also referred to as the mortise joint. The subtalar, or talocalcaneal joint is the articulation between the superior side of the calcaneus and the inferior side of the talus. These two joints together form the Ankle Joint Complex (AJC), which was the joint considered for the purpose of this study. Although the AJC consists of cartilage and several different types of ligaments, this study focusses only on the articulating bones of the joint.

Figure 1 - Anatomy of the Ankle Complex Joint (AJC) [5]

Kinematics of the Ankle

The ankle complex is a six degree-of-freedom joint whose motion can be described in the three planes exclusively associated with it. The joint can translate and rotate freely along the sagittal, coronal, and transverse planes, and does not have any fixed axis of rotation [6].

The sagittal plane contains the dorsi flexion/plantar flexion motion, most of which is attributed to the talocrural joint (about 80%) [7]. The average ROM in this plane is about 60° for the natural ankle without an implant [8]. The coronal plane contains the inversion/eversion motion, and about 60% of this motion is contributed to by the subtalar joint. The ROM is about 60° [8]. The transverse plane contains the internal rotation/external rotation motion, and the motion is split nearly evenly between the talocrural and subtalar joints, and the ROM is about 25° [9].
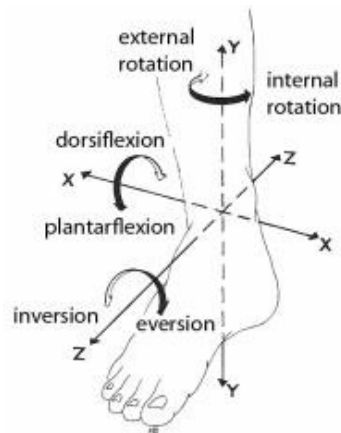
Figure 2 - The degrees-of-freedom of the ankle complex joint [9]

Studies in distance mapping

With the theoretical background in mind, it seems difficult that any research on 3-D deviation between bone surfaces may have been possible without the use of a computational software. However, early studies of the interaction between the articulating surfaces were largely performed by hand, and hence were restrictive in the amount of data that could be retrieved. The works of Lundberg et al. [10] involved the manual mapping of the motion of the talar trochlear surface against the trochlear surface of a stabilized tibia and fibula. The talus, marked with a drilled reference point X, was carried from dorsi flexion through to plantar flexion along a vertically traced reference line. In the four positions of the talus through this range of motion, the distance of the drill point X was measured from the vertical reference line, and these positions were then "traced" to reveal a sequence of motion by means of the displacement of the talus at every position. This study was crucial to observing the change of direction of the oblique axis passing through the talus, as it moves from the neutral position to either extremity. An additional aspect of the study was the observation of the position of the posterior third of the talus, as it moves from dorsi to plantar flexion. By observing the roentgen stereophotogrammetric images of the sagittal cross section of the hindfoot, Lundberg et al. could estimate the amount of contact between the ankle mortise and the talus during the described motion.
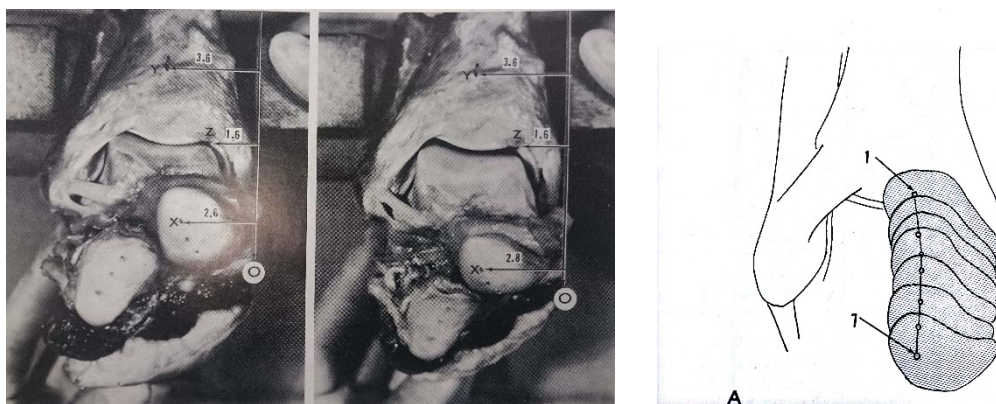
Figure 3 – (left) The talar head in neutral, and then plantarflexion. "O" is the vertical line. Y & Z are tibial reference points, and (right) position of talus traced through dorsi/plantar flexion [10].

Another example of the use of distance mapping was demonstrated by Foumani et al.[11] who performed an in-vivo dynamic and static three-dimensional joint space distance mapping study for the assessment of cartilage thickness in the radiocarpal joint. Using CT scans of the wrist, the team generated static distance maps for each of the positions (poses) of the hand, for the various types of motion of the wrist joint. A value for maximum distance was set, and points on the reference bone were measured from the test bone by means of surface normals, for a set angular value. Combining the static maps gave rise to a dynamic map, which covered the area of interest over all positions, and lead to the determination of the minimal distance to the opposing bone within this field of interest.
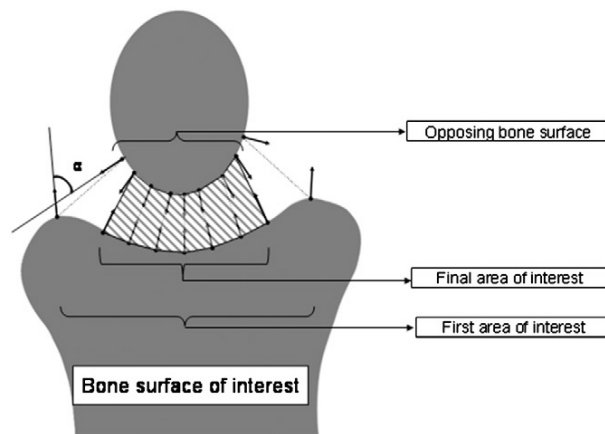
Figure 4 - For each point on the bone surface of interest the closest distance to the opposite target bone surface is found (dotted lines) for a given position and orientation of the opposing bone [11].

Although the technique used by Foumani et al. is similar to this study in concept, it has been observed that not much work has gone into studying the surface-to-surface interaction of the articulating bones of the **ankle complex** specifically. Hence, this study proposes a method to perform surface-to-surface distance mapping for the bones of the ankle joint complex, for the prescribed motions as set forth by the experimental procedure. The goal is to outline a technique for the production of distance maps which will aid in the surface interaction analysis of the bones whilst fit with a TAR model, in order to achieve an implant design with the best human morphological replications.

Theory of distance mapping

To visualize the differences in shape and surfaces, the 3-D compare tool in Geomagic Control™ is used. This tool aids in the creation of colour coded "maps" that depict the 3-D distance between the two models under consideration. This map is thus a graphic representation of a gradient of colours on the reference object. Understanding the theory behind this tool is an essential step in proceeding with the methodology. The critical angle is the maximum angular difference between the normals of two points that suggest they lie on different faces. First, a point on the test object is projected to the Reference object along that test point's known normal vector.

── Reference Object
ᔑ Test Object
→ Normal of Point on Test
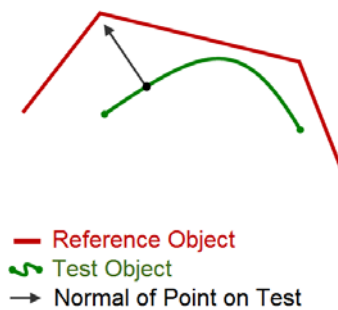
Figure 5 - Theoretical functioning of distance mapping as used in Geomagic Control™

Next, the shortest distance to the reference object is found by checking radially from the test point. The maximum allowable size of this radius is the maximum deviation.

• Closest Point from Test Object

Figure 6 - Explanation of maximum deviation used in 3D deviation analysis in Geomagic Control™

Lastly, to find the critical angle, the normal of the closest point on the reference object is compared

(angular measurement) to that of the normal of the test point.
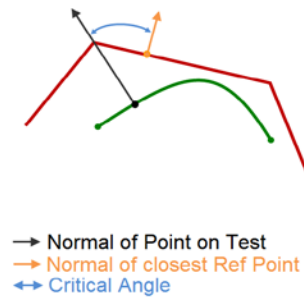
Figure 7 - Final calculation of 3D deviation between the Test and Reference object in Geomagic Control™

If the resulting critical angle value is found to be within the *user specified* critical angle then this reference

point is used. If the value is greater than the specified critical angle then the search radius is increased

until the value meets the *user-defined* Critical Angle or the specified maximum deviation is reached. Thus,

the tool is able to compute the deviation of the test object from the reference object, while the user has

the freedom to alter the angle and the range of values over which this deviation should occur, for

optimum visual results.

CHAPTER 3: METHODOLOGY

Imaging and 3D rendering

The MRI and CT scan data of the ankle of a cadaveric specimen named GAMBA 29, was chosen for the purpose of this study. This data was imported into a commercial image processing software Analyze Direct™ to produce three dimensional numerical renderings of the bones which consisted of the talus, the distal tibia and the distal fibula. The bone renderings were obtained by the process of segmentation, an edge detection algorithm for identifying the boundaries of each bone in each 2D slice, followed by 3D rendering algorithm in which the 2D segmented images were combined to produce surface representation of the aforementioned three bones. The 3D surface renderings were then exported from Analyze Direct™ for use in a commercial 3D CAD and reverse engineering software called Geomagic Control™, where they were slightly smoothed through a spatial filter to remove minor spikes introduced during the segmentation process. All subsequent 2D and 3D processing and measurements were performed in both Geomagic Control™ [12].
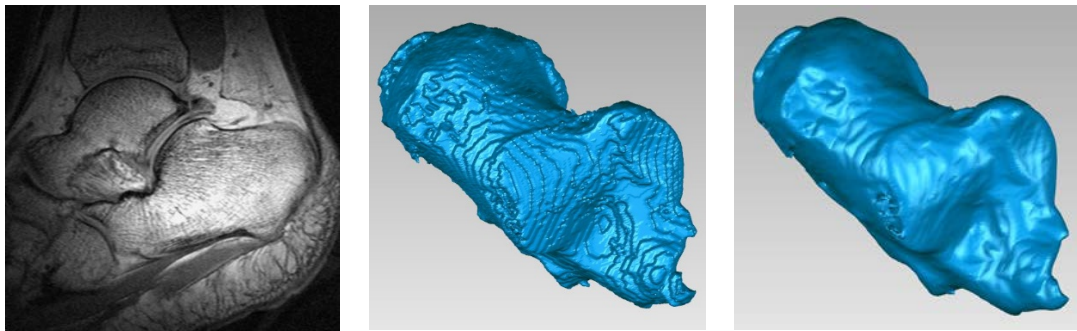
Figure 8 – (left) MRI scan of calcaneus [13]; (center) calcaneus rendering after segmentation; (right) after performing smoothening operation in Geomagic Control™.

Surface generation

The measurements taken in Geomagic Control™ consisted of cross sectional cuts, tibial and talar

reference cutting planes as well as bounding planes, the intermalleolar axis, and best fit circles fitted to

the sections that represent the talar dome at the lateral and medial facets [14], for the purpose of

creating the curvature of the implant models. These measurements were done for each implant type, i.e.,

the Cylindrical, the Inman, and the SSCL (Saddle Shaped truncated Cone with Lateral apex) tibial and talar

implant models. The compiled measurements for each individual implant component were then imported

into Creo Parametric™, where the implant surface design was modeled as a solid, guided by the

measurements taken previously. Once these implants were modeled completely, they were imported into

Geomagic Control™ along with the corresponding bones, which had the appropriate cuts made in order to

accommodate the implant. The implants were attached to the bones, in order to carry out the distance

mapping.
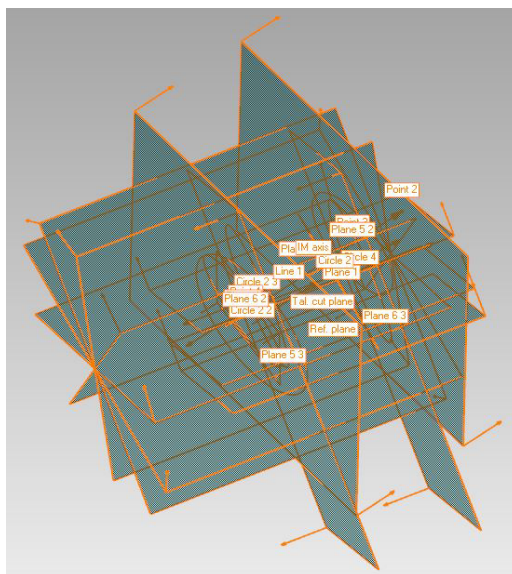
Figure 9 - Compiled geometrical features as obtained from measuring and marking the bones in Geomagic Control™.
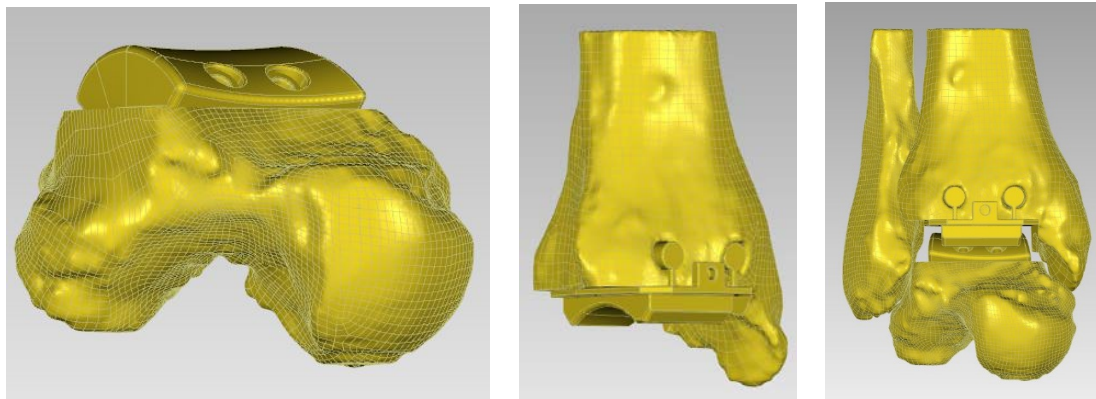
Figure 10 - (left to right) – The trochlear surface of the talus replaced and fit with the SSCL talar implant; the tibial plateau cut and fit with the SSCL tibial implant; the complete assembly as viewed from the anterior side, with the fibula attached.

Experimental procedure

For the purpose of testing, the cadaveric bones fitted with the 3D - printed implants were fixed onto an apparatus referred to as the Ankle Flexibility Tester (AFT) was used. This tester is a six degree-of-freedom linkage, and was used in conjunction with an optoelectronic stereo-photogrammetric motion data acquisition system (Stryker Knee Navigation System, Stryker®, Kalamazoo, MI-USA; nominal accuracy: 0.5 mm and 0.5 degrees). The device provides the capability to apply controlled torques across the ankle complex while measuring the motion produced in response at the ankle, subtalar, and ankle complex.
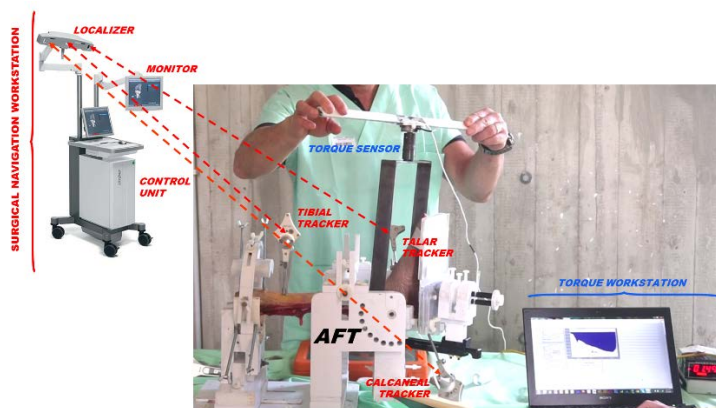
Figure 11 - A cadaveric specimen loaded onto the Ankle Flexibility Tester [13]

Motion was produced at the ankle complex by manually applying torques through an instrumented

torque sensor about the inversion/eversion and internal/external rotation axes of the AFT [15]. These

torques were applied starting from three different joint positions within the flexion arc, i.e. the neutral,

maximum dorsiflexion, and maximum plantarflexion positions. At least four loading-unloading cycles were

applied in each test at a slow rate of approximately 5 cycles per minute. Simultaneously, an

optoelectronic system was utilized to track the motion of the three bones (tibia, talus, and calcaneus).

This system consisted of a camera sensor and a computer with dedicated software, and four trackers

(fiduciary markers) with 5 light-emitting-diodes each, capable of recording the motion of a rigid body

object in space. Three fiduciary markers were securely fixed to the tibia, talus and calcaneus each, to

record their corresponding motion. The fourth tracker was used for system control and landmark

digitization.

The testing procedure was concluded by the digitization of the fiduciary markers and of a number of

anatomical landmarks which included the tibial tuberosity and the two malleoli, the four corners on the

talar cut, and on the calcaneus, the Achilles's tendon insertion, the central plantar and the most

prominent lateral facet [16].

<u>Analytical procedure</u>

The digitized anatomical landmarks were used to establish anatomical reference frames for the

tibia/fibula, talus, and calcaneus [17] and the motion between these frames was used to assess

kinematics at the tibio-talar (Ankle), talo-calcaneal (Subtalar), and tibio-calcaneal (Complex) joints. For

each of these joints, dorsiflexion/plantarflexion, inversion/eversion, and internal/external rotation were

calculated according to a joint coordinate system convention [18]. Primary kinematics were defined as the

joint rotation produced in the direction of the applied torque.

The focus of this study was the kinematics of the tibio-calcaneal (complex) joint. For the given torque

applied, the positions of the three fiduciaries from each bone and the joint rotation angle was recorded at

various time steps, and was tabulated. The processing of this data was done using multiple commercial softwares, in the same sequence as explained below:

The fiduciary marker position data was processed to obtain graphical representations (plots) of the change in angle with every time step. The joint rotation angle associated with the ankle complex is denoted as follows, for the three different types of motion:

1. Alpha (α) for Dorsi flexion/Plantar flexion

2. Beta (β) for Inversion/Eversion

3. Gamma (γ) for Internal rotation/External rotation

The values of the angles were *corrected* so as to make the value of the angle corresponding to the first time step, zero. This was done for all the different configurations of the cadaveric specimen w.r.t the type of motion being considered, the type of implant under test, as well as its start position in the AFT. To elucidate, this means that, for a configuration such as **DPSN**, the cadaveric specimen was moved through **D**orsiflexion/**P**lantarflexion, fitted with the **S**SCL implant models, and its motion was recorded starting from the **N**eutral position.
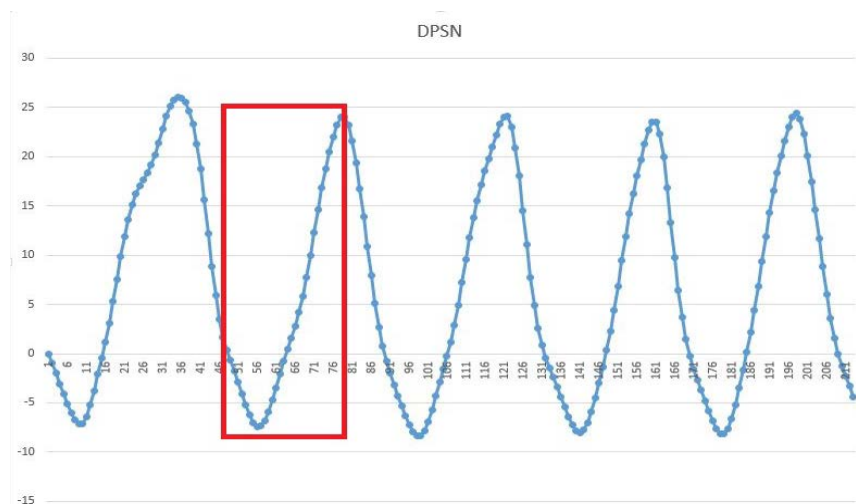
Figure 12 - Graph of α plotted for DPSN. The highlighted box indicates the second cycle, the points of which were used for calculating the distance maps.

The tabulated point data was then run through a Python™ code, which picked up the fiduciary coordinates for the extremities in position of the second cycle for every configuration, through the loading/unloading of the specimen, i.e., for the points corresponding to the maximum dorsiflexion, maximum plantarflexion, and two neutral points.

The 3D renderings of the bones fitted with the implants, were imported into Geomagic Control™, into the same file that contained the position data from the previous step.

When the renderings were obtained from the MRI scans, they were devoid of any fiduciaries marked on them. However, they contained the same indentations as the actual bones, from the landmarks where the fiduciaries were physically fitted into them during testing.
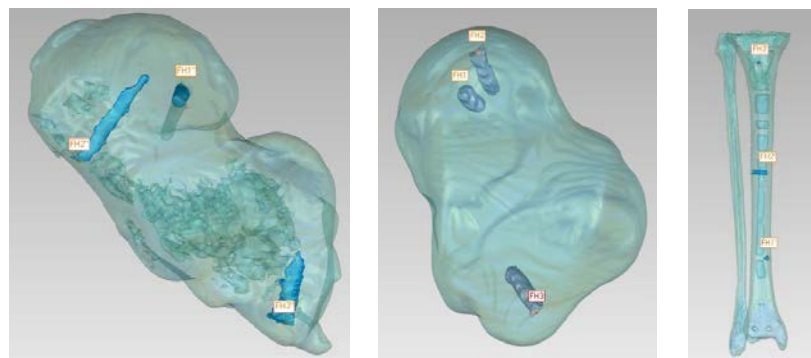
Figure 13 - (left to right) – The bones with the fiduciary landmarks and corresponding points.

Using these, it was possible to denote the original locations of the three fiduciaries on each bone, which were in their own local frame of reference. Since the AFT has its own surgical navigation coordinate system, the positions at every time step were recorded in a different frame of reference. A frame of reference that of Geomagic Control™, also existed simultaneously with the other two systems. For the purpose of computation, it was acceptable to neglect the transformation between the AFT's surgical navigation system, and the Geomagic Control™ global coordinate system. Importing the renderings into Geomagic Control™ thus implied that a transformation had to be made between the local frame of reference of the bones, and that of Geomagic Control™ itself. In order to do this, the talus was used as a control for the first transformation or *alignment*.

Reference Point System (RPS) Alignment

In Geomagic Control™, the RPS Alignment tool is the alignment of a Test and Reference object by declaring a set of corresponding points on each, and by constraining each pair of points in a single direction. The 3D space in Geomagic Control™ containing the fiduciary points was made the Reference, and the initial 3D rendering of the talus was made the Test object. The fiduciaries from the talus were then aligned to the positions corresponding to the first time step, at the beginning of the second cycle.
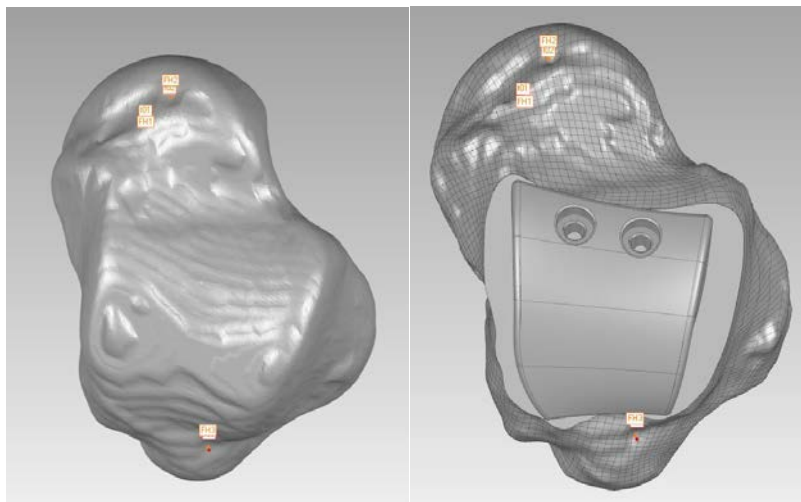
Figure 14 - Fiduciaries on the Natural Talus (left) and SSCL Talus (right) aligned with the points of the first time step, with a minimal error.

Best Fit Alignment

Once the RPS alignment was completed, another copy of the talus was imported into Geomagic Control™ and a best fit alignment was performed, to obtain an optimally positioned talus, which was completely transformed from the local bone coordinate system to the Geomagic Control™ global coordinate system.

The best fit alignment in Geomagic Control™ uses an Iterative Closest Point algorithm (ICP). The Test and Reference objects are brought into a roughly aligned (matched) position. The Test object is then sampled and the closest points are computed on the Reference to each sample point based on the sample size

selected in the command. Next, a least-squares method is employed, where the sums of squares of distances between the sample pairs are minimized over all the rigid motions that could realign the two objects. Having done this, Geomagic Control™ re-computes the closest points on the reference and establishes a new transformation matrix. This iterative method allows for the Sample Size and Tolerance to be toggled. For the purpose of this study, the Sample Size was maintained at 1500, which means that these were the number of random points on the test model to align to corresponding points on the reference model. The Tolerance, which controls the average tolerance at which best fit goes from its gross alignment algorithm to the fine adjustment algorithm, was maintained at 0.51076 mm. Both these values were the default, as computed by Geomagic Control™ and were acceptable for aligning the talus.
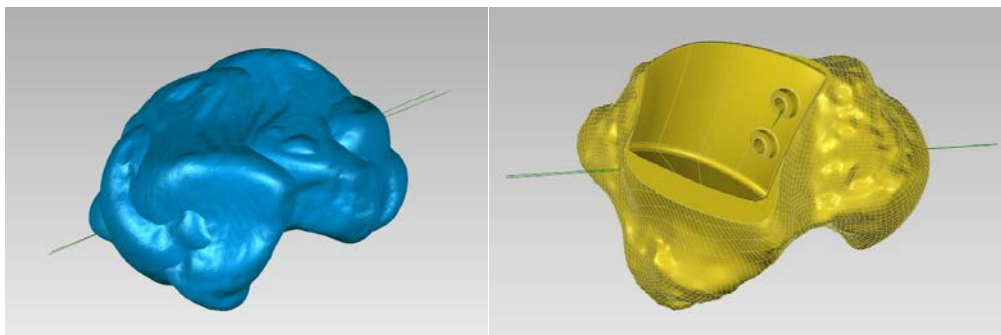
Figure 15 - Best Fit Alignment performed on the Natural talus (left) and the SSCL Talus (right), with an average error of 0.000014 mm as compared between a talus with an implant, and one without.

Once the talus was aligned to its copy using this feature, a transformation matrix was made available, which was used to transform the positions of the other two bones, i.e., the tibia/fibula and the calcaneus.
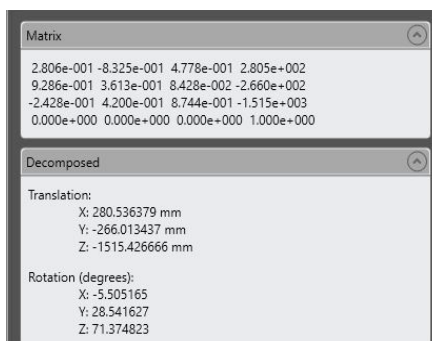
Figure 16 - The resulting transformation matrix, as seen for the DPNN case.

CHAPTER 4: RESULTS

Primary motion classification

The distance mapping was done on the ankle joint (tibia/fibula and talus) and the subtalar joint (calcaneus and talus), alternating each bone in the pair under consideration, as the Test and Reference object. The procedure was performed for three different classes of implants and on the natural bones without an implant. Under each of these classes, there were seven cases of movement analyzed, which were combinations of varying initial positions on the AFT and the type of ankle motion. The following table depicts this classification clearly:

Table 1 - Implant and motion classification.

Natural	Inman	Cylindrical	SSCL
DPNN	DPIN	DPCN	DPSN
INTNN	INTIN	INTCN	INTSN
INTND	INTID	INTCD	INTSD
INTNP	INTIP	INTCP	INTSP
INVNN	INVIN	INVCN	INVSN
INVND	INVID	INVCD	INVSD
INVNP	INVIP	INVCP	INVSP

Each of the abbreviations stand for three different parameters. As an example, in the case of the SSCL implants:

1. **DPSN** – motion of **D**orsi flexion/**P**lantar flexion, with a **S**SCL implant, the bone displacement starting from the **N**eutral position.

2. **INTSD/INVSD** – motion of **I**nternal rotation/External rotation, or **I**nversion/Eversion, with a **S**SCL implant, the bone displacement starting from initial **D**orsi flexion.

3. **INTSP/INVSP** – motion of **I**nternal rotation/External rotation, or **I**nversion/Eversion, with a **S**SCL implant, the bone displacement starting from initial **P**lantar flexion.

Kinematics

Distance mapping was carried out on both the talocrural and the subtalar joints. The articulating bones, once imported into Geomagic Control™, had a clearance of approximately 2 mm between them, where the cartilage would have been. The study was conducted by isolating the bones entirely, by excluding all ligament and the cartilage as well. This was done mainly to reduce computational complexity.

As seen in an earlier section, the 3D Compare tool in Geomagic Control™ generates a three dimensional, color-coded mapping of the differences between the selected object and one that is chosen by the user. The Test object can be a point, polygon, or CAD object and the Reference object can be a polygon or CAD object. If a portion of the test object has insufficient data for valid comparison to the Reference object, that portion of the Result object is gray. This can be observed from the distance maps as compiled. The percentage of distribution of the colour gradient on the Result object is dependent on the critical angle and maximum deviation as input by the user, and the generic surface irregularities of the two objects under comparison. The patterns obtained in Geomagic Control™ are accompanied by a colour scale, which is akin to a thermal heat map, with the lower end of the spectrum indicating minimal distance or penetration, and the upper end indicating maximum deviation/displacement. The deviation type in Geomagic Control™ was set as the 3D deviation, in which the shortest distance from the Test to any point on the Reference is reported as the result [19].
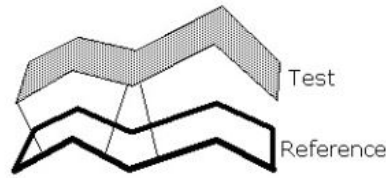
Figure 17 - 3D deviation in Geomagic Control™

When the results for the distance mapping were generated, the Statistics group displayed the following parameters with their corresponding numeric entries:

1. **Maximum Distance** – the greatest deviations that are found anywhere in the comparison, not exceeding the maximum deviation value.

2. **Average Distance** – the average deviation that is found anywhere in the comparison.

3. **Standard Deviation** – the standard deviation of all deviations.

By setting the critical angle at 180^0, the radial distance from any point on the Test object to the Reference object was ensured to be the shortest distance between the two objects. The angular constraint on the 3D deviation was eliminated, and this meant that the shortest distance calculated was along both Test and Reference normals. Thus, the distance between the two objects was reported without much error.

Joint behaviour

For the purpose of this study, the focus of the distance mapping results was mainly on the talocrural joint, in order to observe the differences in deviations for the natural, no-implant case, as against the implant fit bones. The Critical range was maintained at -1 mm to +4 mm, and the nominal range was maintained at -0.25 mm to +0.25 mm. The critical angle was set to 180^0, and the spectrum consisted of 23 colours.

Dorsi flexion – Plantar flexion (DP)

The distance maps for the DP motion displayed some similarities between the DPSN and DPIN cases, in terms of the amount of medial lift-off observed during dorsi flexion, and posterior-lateral dig of the talus into the tibial plateau during plantar flexion. In contrast, the DPCN case displayed more anterior-medial lift off of the talus during plantar flexion, and the DPNN case did not display much difference between the neutral position and the extremities.
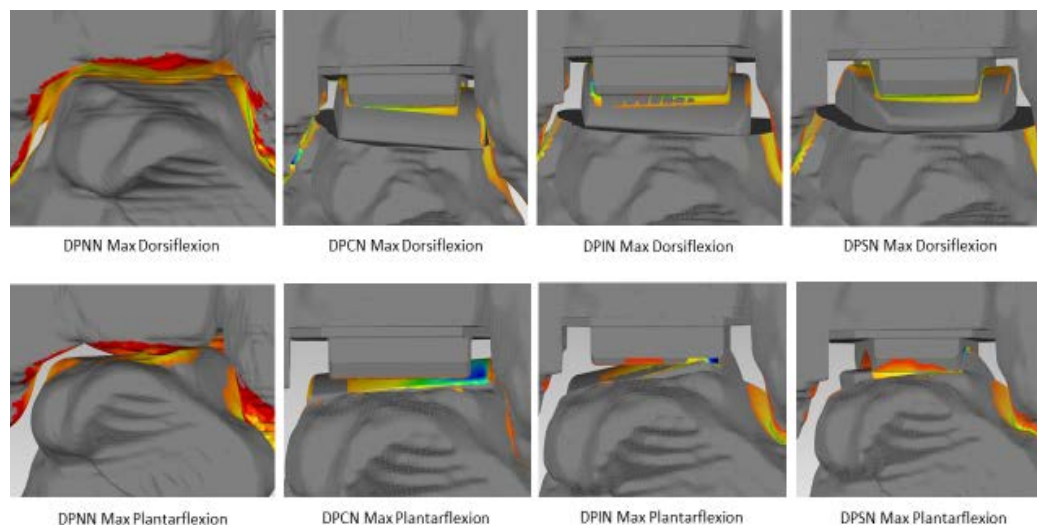
Figure 18 - Dorsi flexion/ Plantar flexion observed in the talocrural joint.

Inversion – Eversion (INV)

The INVIN case displayed motion of the talus away from the lateral side (fibula) during maximum inversion. For INVNN, as the motion went from neutral to maximum inversion, most of the significant motion was actually observed at the subtalar joint, but during maximum eversion, the posterior-lateral side of the talus displayed digging into the fibula. The INVSN case displayed a tight fit of the implant pair during the neutral time steps, but a clear transition was observed along the saddle of the talar implant as the joint moved from inversion to eversion. The INVCN

case looked like a cross between the INVSN and INVIN cases; however, what was unique was that nearly the same amount of liftoff was observed during inversion on the lateral side, as was during eversion on the medial side.

The INVCD case displayed slight lift off of the talus on the lateral side during maximum inversion. The second neutral time step and the maximum eversion position showed almost an equal amount of deviation, with the posterior side of the talus digging into the tibial plateau during maximum eversion. For the INVID case, an almost equal deviation was noticeable on the anterior-medial side for maximum inversion, as was on the posterior-lateral side for maximum eversion. The INVND and INVSD cases showed very similar results from the transition between neutral to each of the maximum positions; there was not much difference in the amount of deviation, which was a near constant within the nominal range. The INVSD as well as the INVSP cases displayed deviational and contact transfer along the saddle of the talar implant from maximum inversion to eversion. In contrast, the INVIP showed a medial dig of the tibia into the talus during both, maximum inversion as well as eversion.

INVNN Max Inversion   INVCN Max Inversion   INVIN Max Inversion   INVSN Max Inversion

INVNN Max Eversion   INVCN Max Eversion   INVIN Max Eversion   INVSN Max Eversion
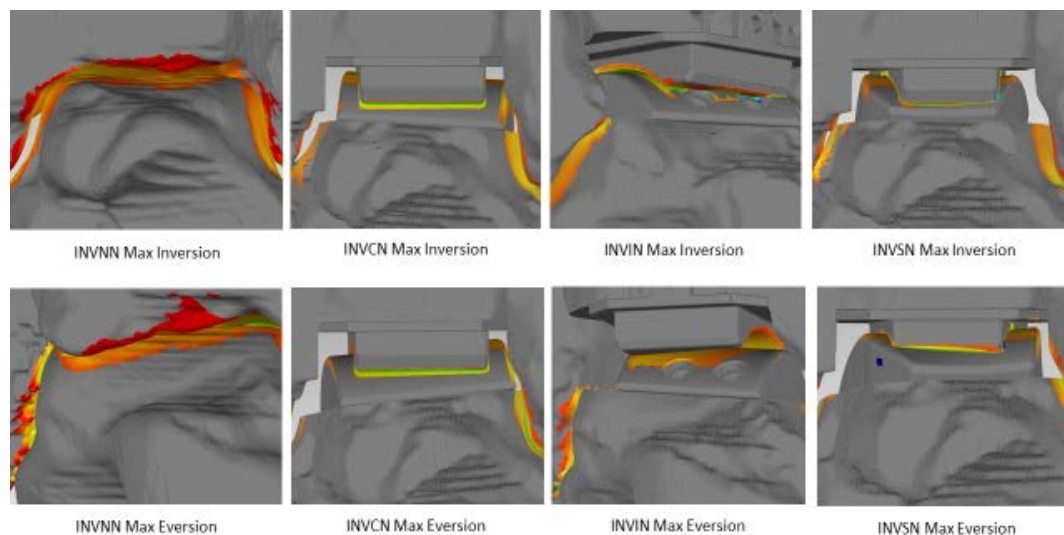
Figure 19 - Inversion/Eversion observed in the talocrural joint.
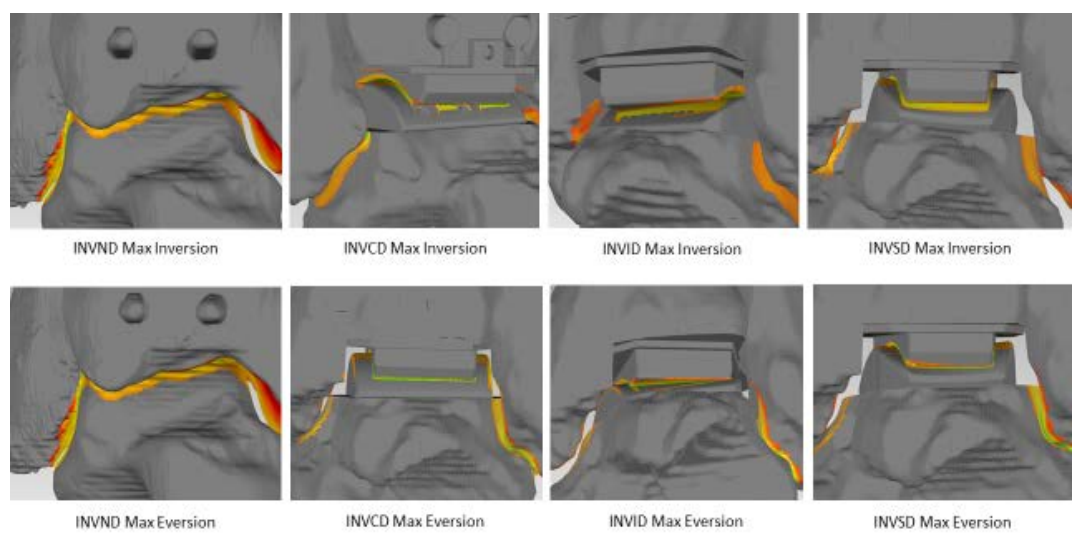
Figure 20 - Inversion/Eversion starting from dorsi flexion, observed in the talocrural joint.
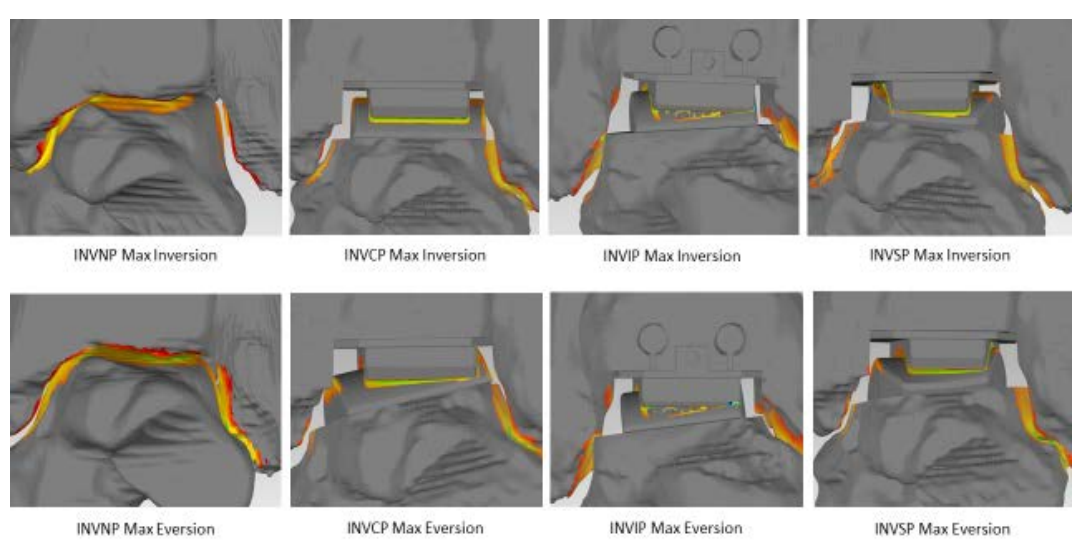
Figure 21 - Inversion/Eversion starting from plantar flexion, observed in the talocrural joint.

Internal rotation – External rotation (INT)

In INTNN, the medial side of the talus came closer to the tibial plateau on the posterior side during maximum internal rotation. However, medial liftoff was observed during maximum internal rotation in the INTSN case. An equal amount of posterior-lateral digging was observed during both maximum internal as well as maximum external rotation. The INTIN case displayed a thin region of digging in on the posterior side during maximum internal rotation, and a good amount of the same deviation behavior on the anterior-medial side during maximum external rotation. The INTCN case did not display much action at the talocrural joint in itself, but some amount of digging in was observed during both extremities of rotation.

When the joint motion was started with an initial of either dorsi flexion or plantar flexion, a varied set of observations was made. The INTND case showed significant stress on the fibula while moving from initial dorsi flexion to maximum internal rotation. The INTNP case showed the talus move a significant amount out of the ankle mortis. For INTID, maximum internal rotation was seen to be highly plantar flexed, whereas the INTIP case produced distance maps which could not be interpreted well even from one neutral position to the next extremity. Finally, the INTSD case displayed an almost even displacement for each of the anterior and posterior halves of the talus, during maximum internal rotation. Maximum external rotation for INTSD showed significant digging in of the talus into the tibial plateau, on the anterior-medial side.

INTNN Max Internal Rotation   INTNN Max Internal Rotation   INTNN Max Internal Rotation   INTNN Max Internal Rotation

INTNN Max External Rotation   INTCN Max External Rotation   INTIN Max External Rotation   INTSN Max External Rotation
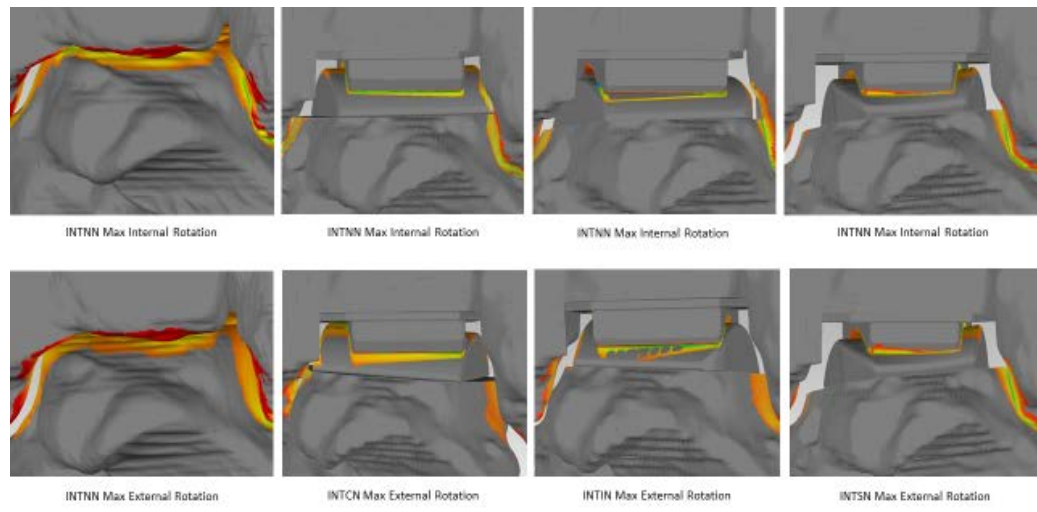
Figure 22 - Internal rotation/External rotation observed in the talocrural joint.

INTND Max Internal rotation   INTCD Max Internal rotation   INTID Max Internal rotation   INTSD Max Internal rotation

INTND Max External rotation   INTCD Max External rotation   INTID Max External rotation   INTSD Max External rotation
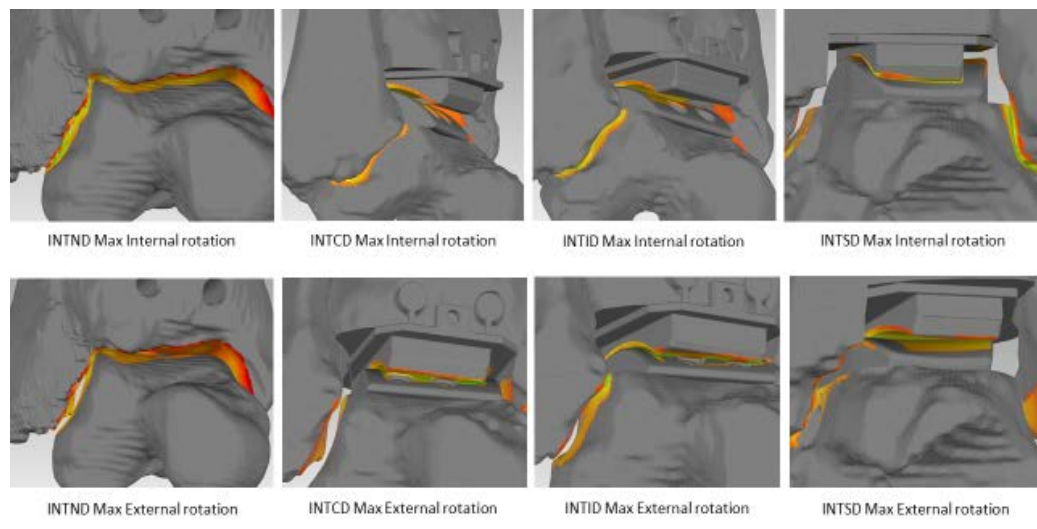
Figure 23 - Internal rotation/External rotation starting from dorsi flexion, observed in the talocrural joint.

INTNP Max Internal rotation   INTCP Max Internal rotation   INTIP Max Internal rotation   INTSP Max Internal rotation

INTNP Max External rotation   INTCP Max External rotation   INTIP Max External rotation   INTSP Max External rotation
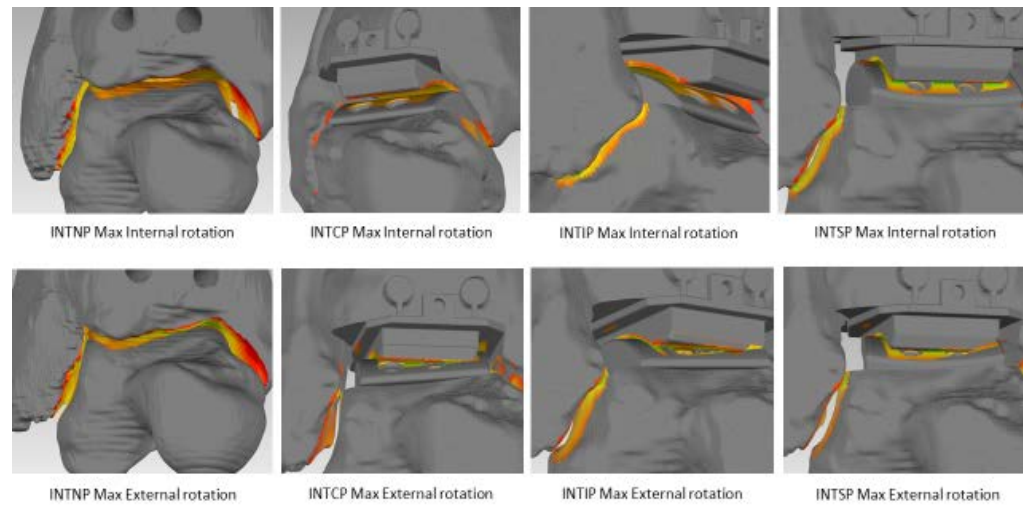
Figure 24 - Internal rotation/External rotation starting from plantar flexion, observed in the talocrural joint.

Distance maps

The following section contains the visual distance mapping data from each of the 28 cases. Each frame was divided into four columns, for each of the four points of the cycle: Neutral, maximum motion in one direction, neutral, and maximum motion in the opposite direction. The tibia and the talus contain additional views from the lateral side, and this was done to observe the motion of the lateral process of the talus against the fibula. The images are arranged in the following implant class sequence:

1. Natural (no implant)

2. Cylindrical implant

3. Inman implant

4. SSCL implant

The deviation spectrum is indicative of the numeric value of the displacement observed. The bones in each frame have been arranged in the manner that they would be exposed, if the joint was *unfolded*, i.e., the face of the calcaneus formed by the posterior articulating surface and the sustentaculum tali, articulates with the bottom surface of the talus, as seen from the bottom two images in any frame. This forms the subtalar joint. The top two images depict the tibial plateau and the talar dome, which fit into one another to form the talocrural joint. The talus and tibia are also pictured from their lateral facets, since the fibula forms the lateral side of the entire complex, and articulates with the lateral process of the talus.
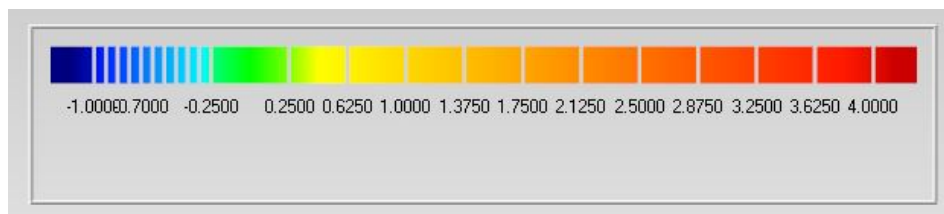
Figure 25 – The deviation spectrum in Geomagic Control™

DPNN – T.S 39 (Neutral position)   DPNN – T.S 47 (Maximum Dorsi flexion)   DPNN – T.S 53 (Neutral position)   DPNN – T.S 68 (Maximum Plantar flexion)
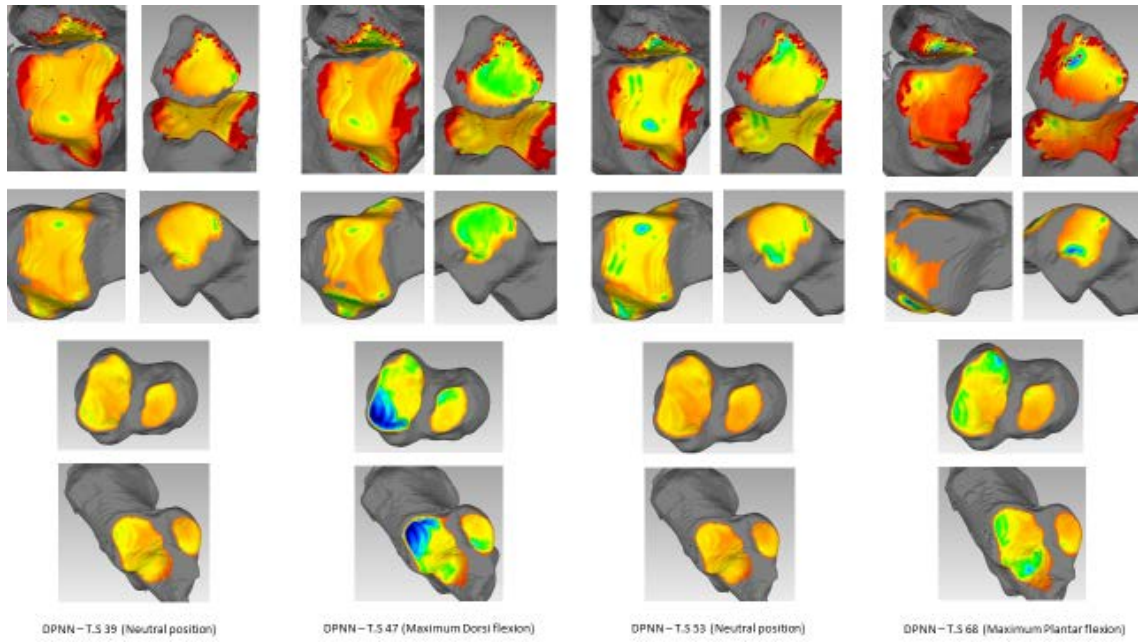
Figure 26 - DPNN - Dorsiflexion/Plantarflexion Natural Neutral.

INTND – T.S 48 (Dorsi flexion)   INTND – T.S 61 (Maximum Internal Rotation)   INTND – T.S 68 (Dorsi flexion)   INTND – T.S 80 (Maximum External Rotation)
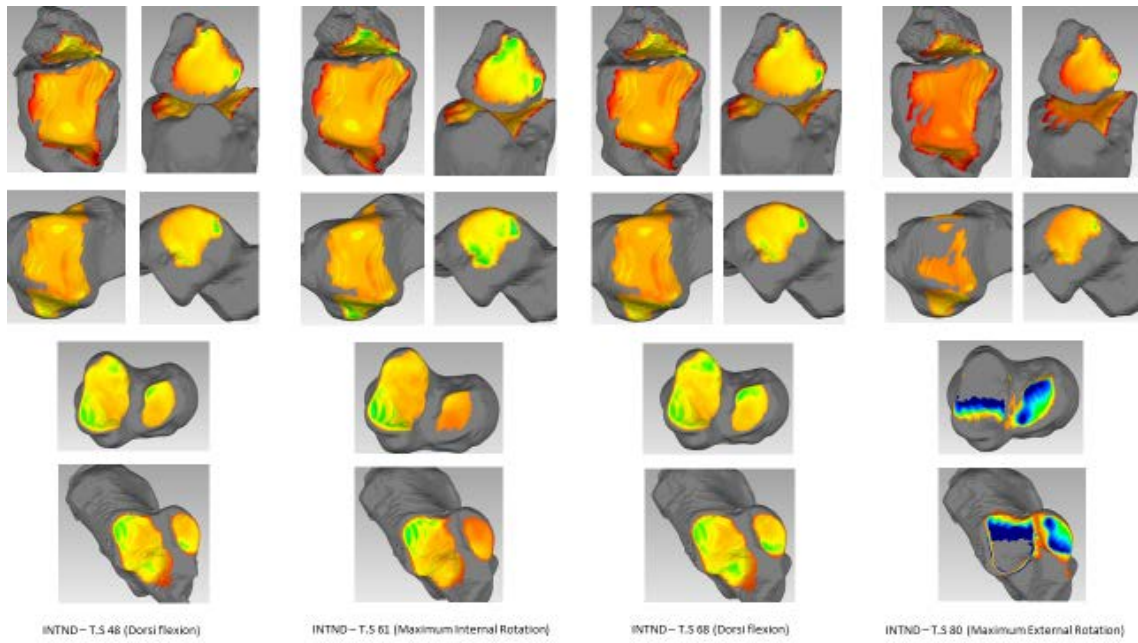
Figure 27 - INTND - Internal rotation/External rotation Natural Dorsiflexion

INTNN – T.S 45 (Neutral position)   INTNN – T.S 61 (Maximum Internal Rotation)   INTNN – T.S 71 (Neutral position)   INTNN – T.S 81 (Maximum External Rotation)
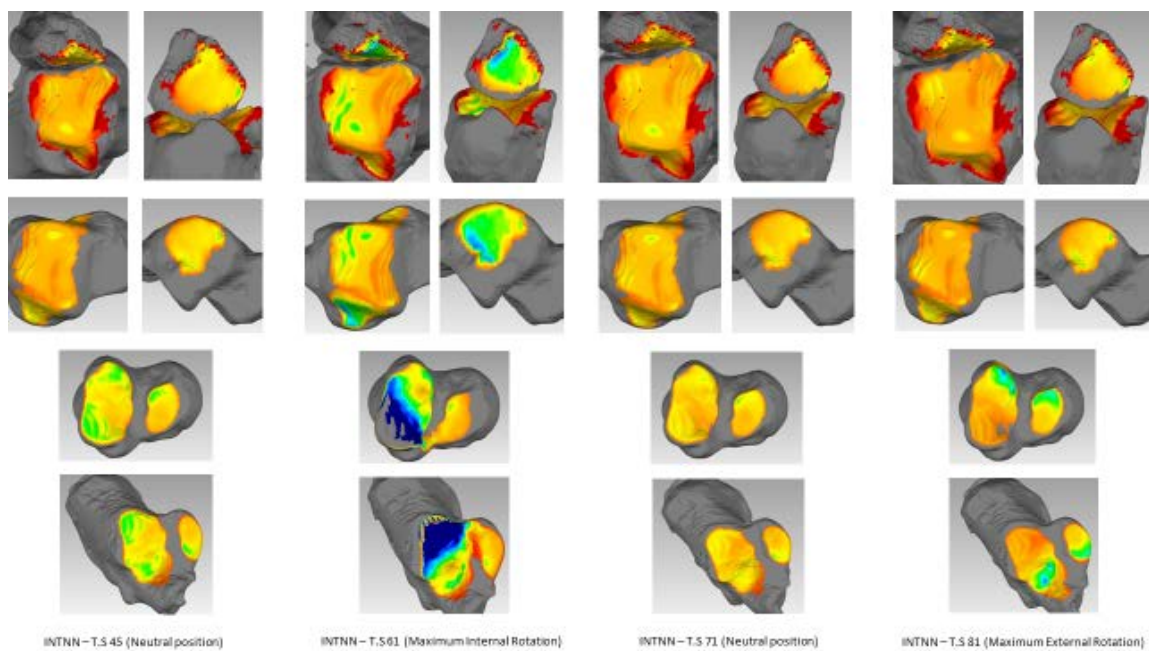
Figure 28 - INTNN - Internal rotation/External rotation Natural Neutral

INTNP – T.S 50 (Plantar flexion)   INTNP – T.S 63 (Maximum Internal Rotation)   INTNP – T.S 85 (Plantar flexion)   INTNP – T.S 85 (Maximum External Rotation)
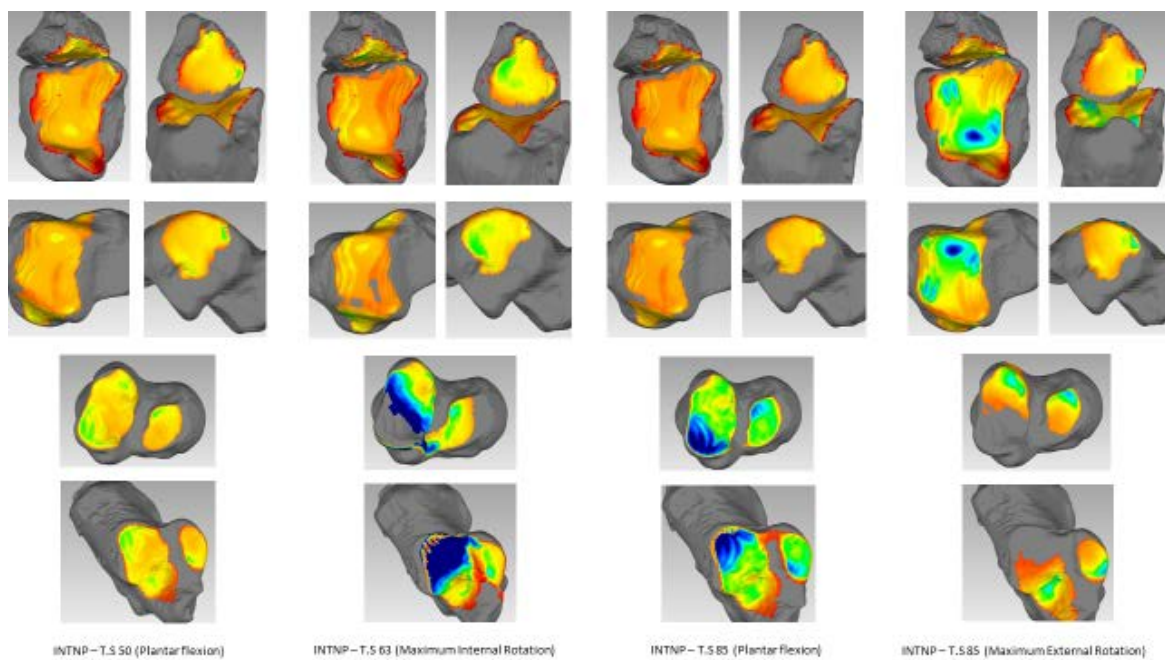
Figure 29 - INTNP - Internal rotation/External rotation Natural Plantarflexion

INVND–T.S 20 (Dorsi flexion)   INVND–T.S 26 (Maximum Inversion)   INVND–T.S 32 (Dorsi flexion)   INVND–T.S 35 (Maximum Eversion)
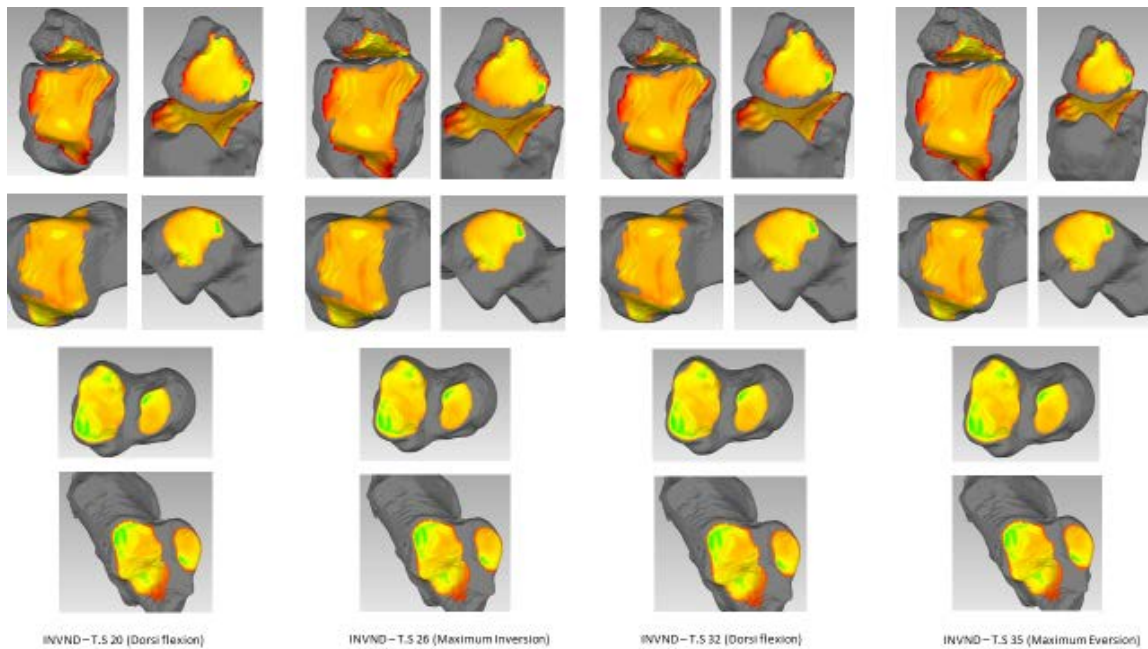
Figure 30 - INVND - Inversion/Eversion Natural Dorsiflexion

INVNN–T.S 29 (Neutral position)   INVNN–T.S 37 (Maximum Inversion)   INVNN–T.S 44 (Neutral position)   INVNN–T.S 51 (Maximum Eversion)
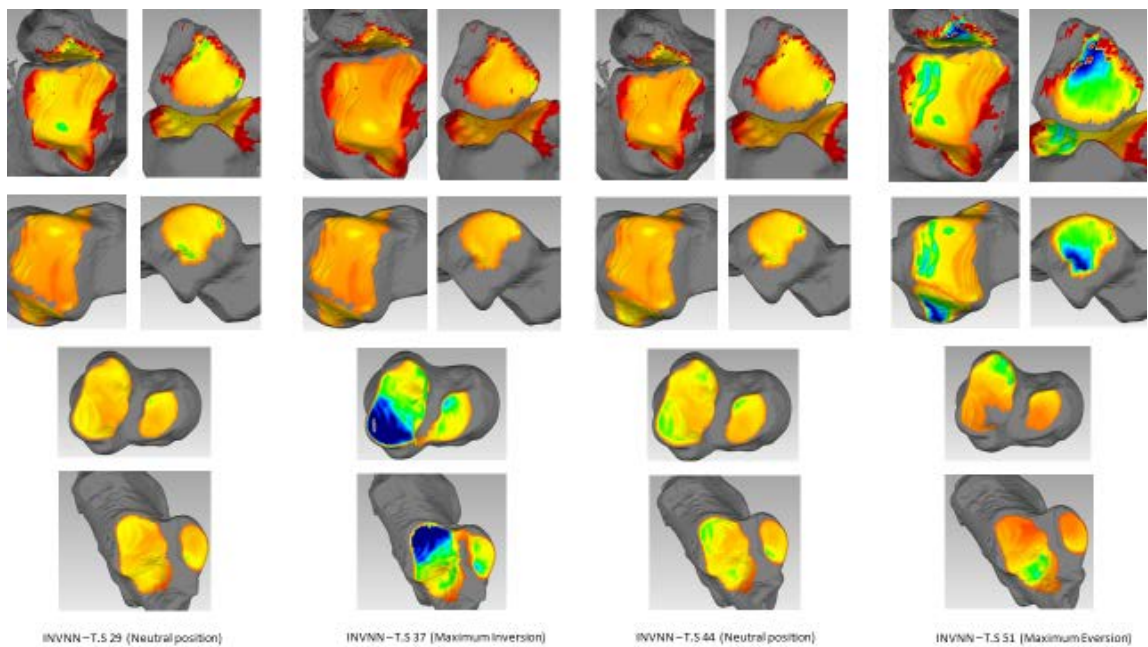
Figure 31 - INVNN - Inversion/Eversion Natural Neutral

INVNP−T.S 32 (Plantar flexion)   INVNP−T.S 43 (Maximum Inversion)   INVNP−T.S 52 (Plantar flexion)   INVNP−T.S 60 (Maximum Eversion)
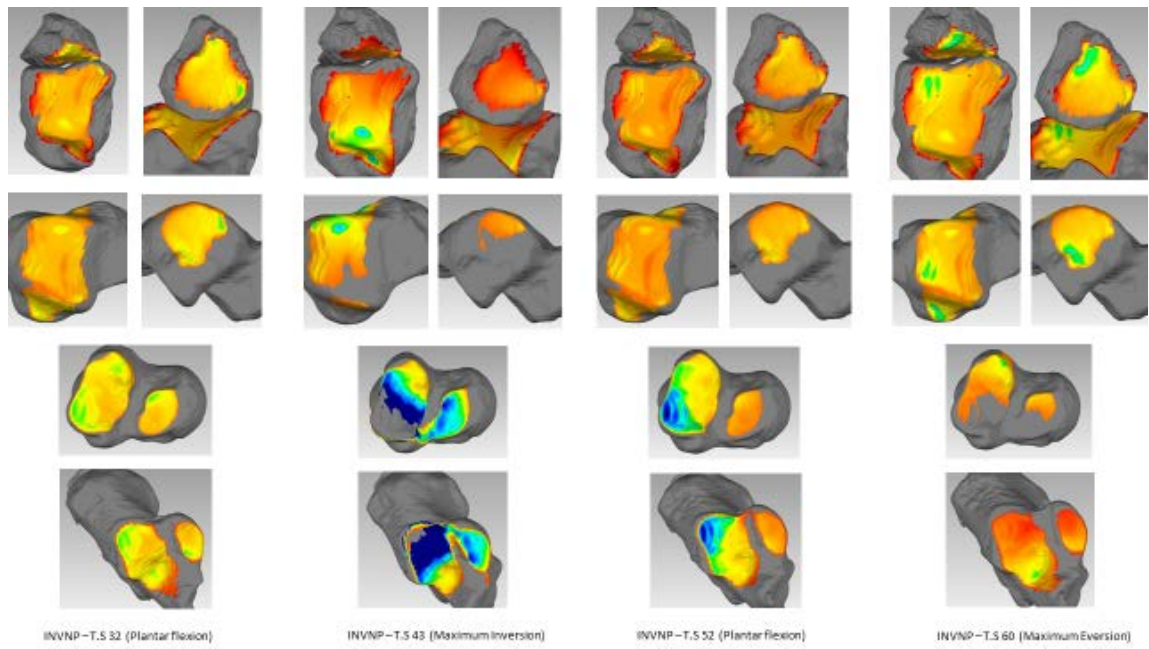
Figure 32 - INVNP - Inversion/Eversion Natural Plantarflexion

DPCN – T.S 36 (Neutral position)   DPCN – T.S 46 (Maximum Dorsi flexion)   DPCN – T.S 56 (Neutral position)   DPCN – T.S 65 (Maximum Plantar flexion)
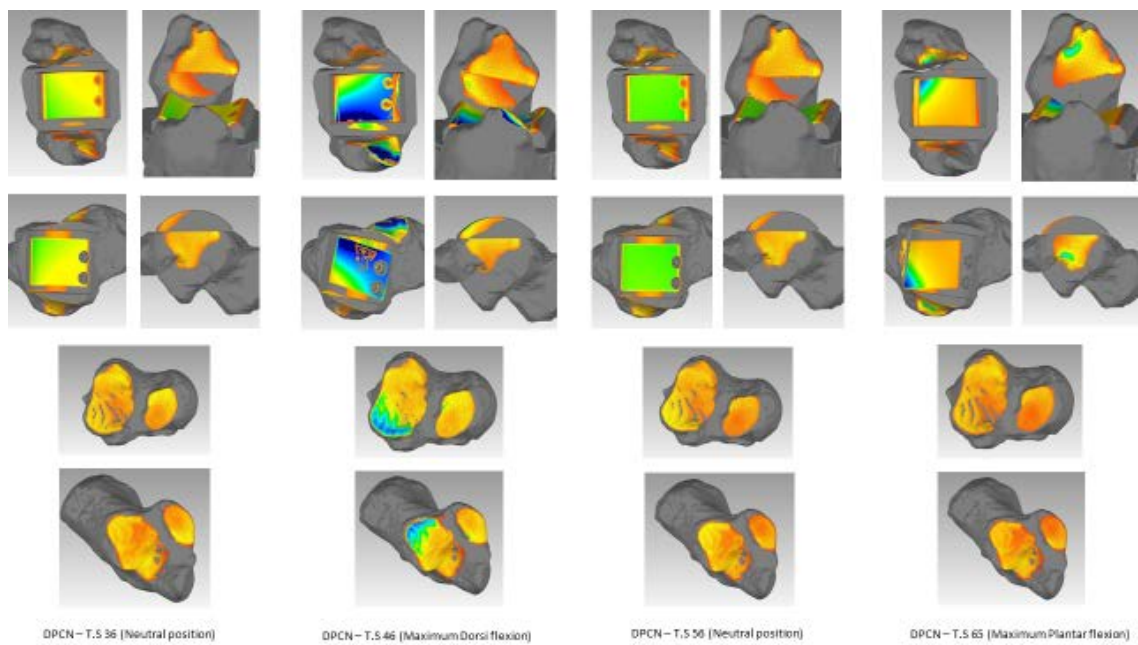
Figure 33 - DPCN - Dorsiflexion/Plantarflexion Cylindrical Neutral

INTCD – T.S 41 (Dorsi flexion)   INTCD – T.S 53 (Maximum Internal Rotation)   INTCD – T.S 61 (Dorsi flexion)   INTCD – T.S 72 (Maximum External Rotation)
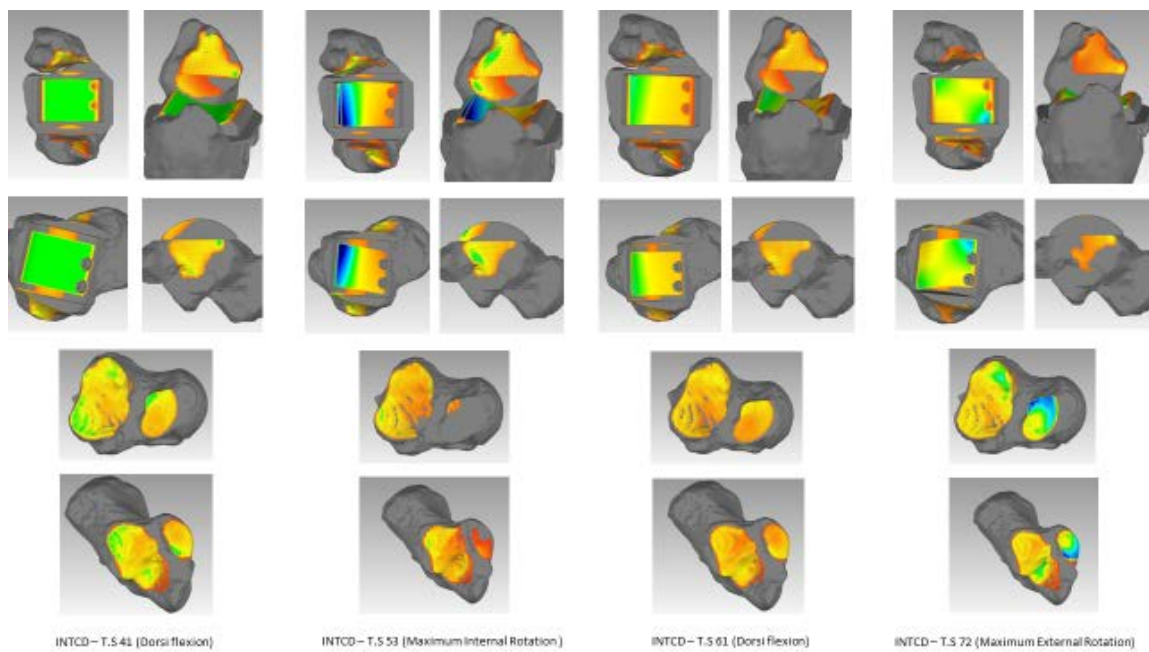
Figure 34 - INTCD - Internal rotation/External rotation Cylindrical Dorsiflexion

INTCN – T.S45 (Neutral position) INTCN – T.S57 (Maximum Internal Rotation) INTCN – T.S64 (Neutral position) INTCN – T.S 74 (Maximum External Rotation)
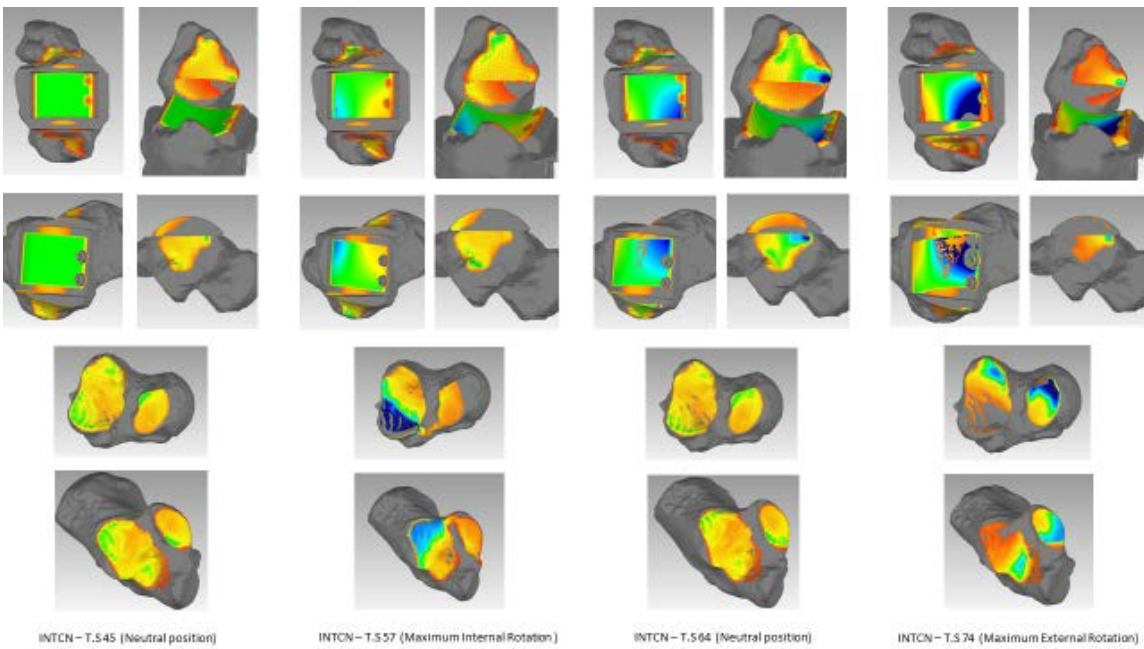
Figure 35 - INTCN - Internal rotation/External rotation Cylindrical Neutral

INTCP – T.S41 (Plantar flexion) INTCP – T.S53 (Maximum Internal Rotation) INTCP – T.S62 (Plantar flexion) INTCP – T.S 74 (Maximum External Rotation)
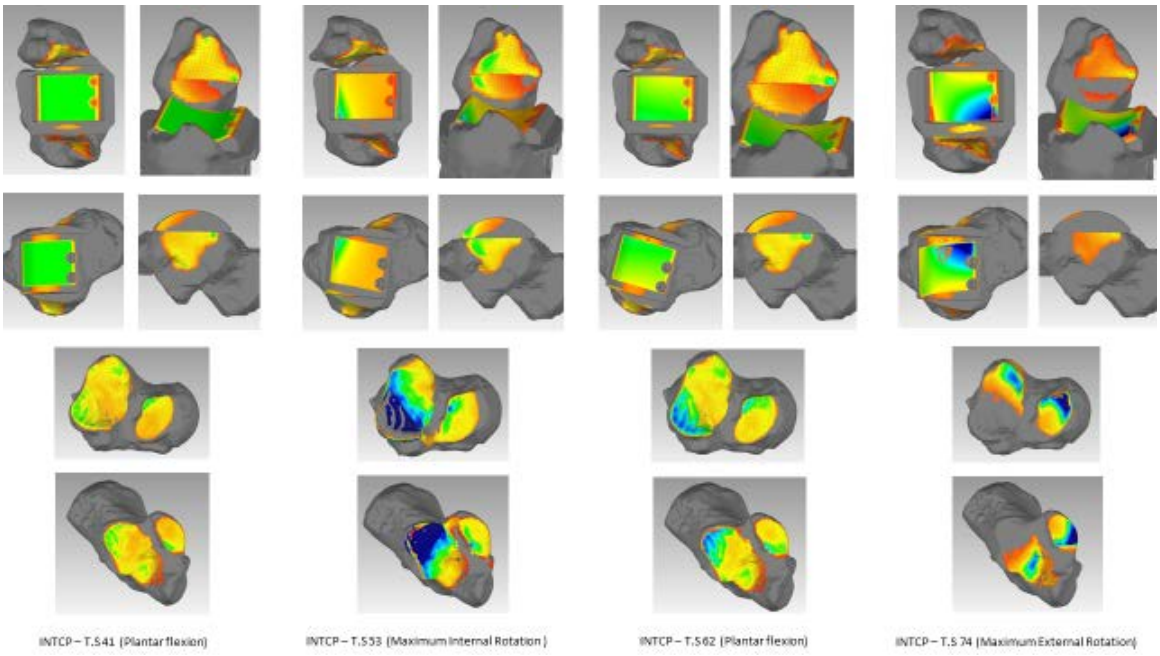
Figure 36 - INTCP - Internal rotation/External rotation Cylindrical Plantarflexion

INVCD – T.S 31 (Dorsiflexion)   INVCD – T.S 39 (Maximum Inversion)   INVCD – T.S47 (Dorsiflexion)   INVCD – T.S 51 (Maximum Eversion)
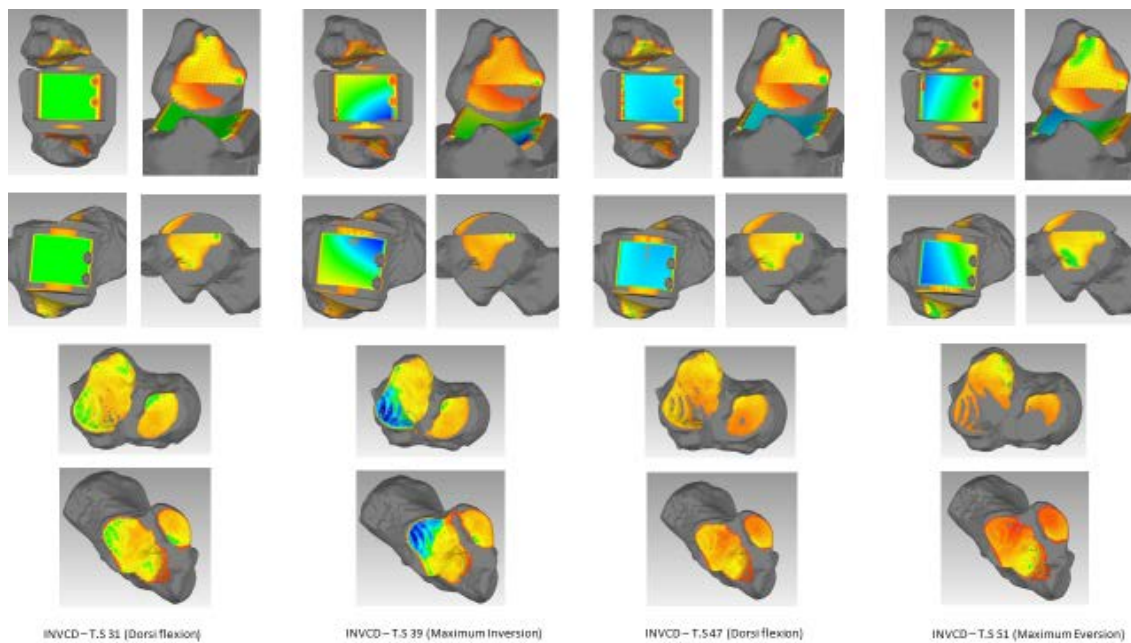
Figure 37 - INVCD - Inversion/Eversion Cylindrical Dorsiflexion

INVCN – T.S 32 (Neutral position)   INVCN – T.S 40 (Maximum Inversion)   INVCN – T.S 46 (Neutral position)   INVCN – T.S 52 (Maximum Eversion)
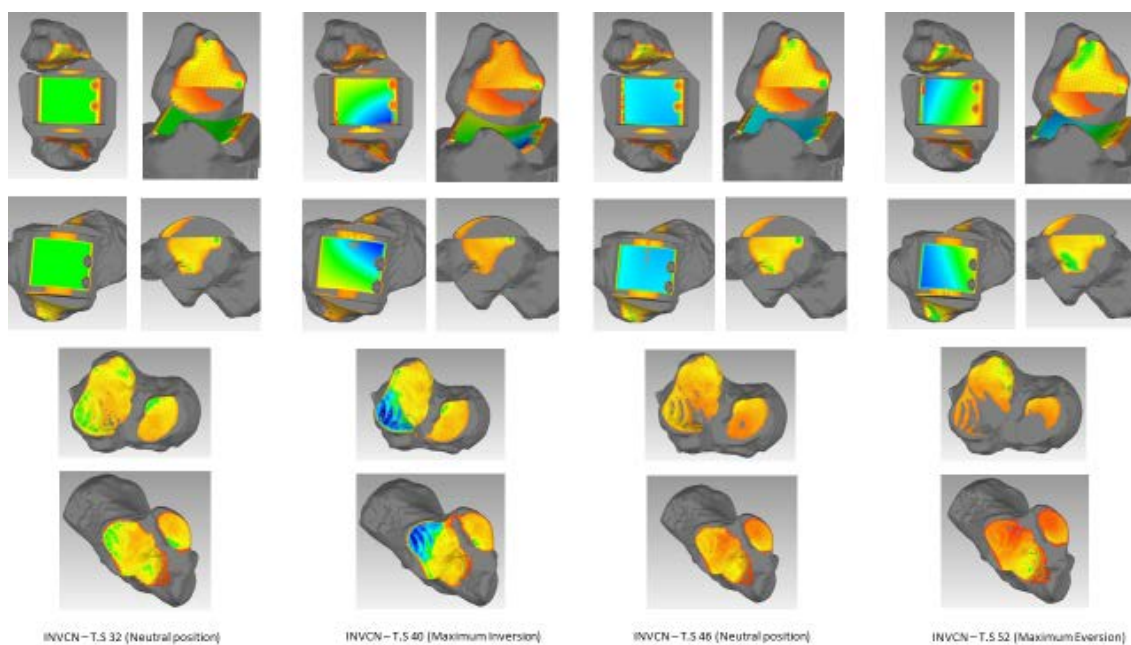
Figure 38 - INVCN - Inversion/Eversion Cylindrical Neutral

INVCP – T.S 31 (Plantar flexion)   INVCP – T.S 32 (Maximum Inversion)   INVCP – T.S 33 (Plantar flexion)   INVCP – T.S 46 (Maximum Eversion)
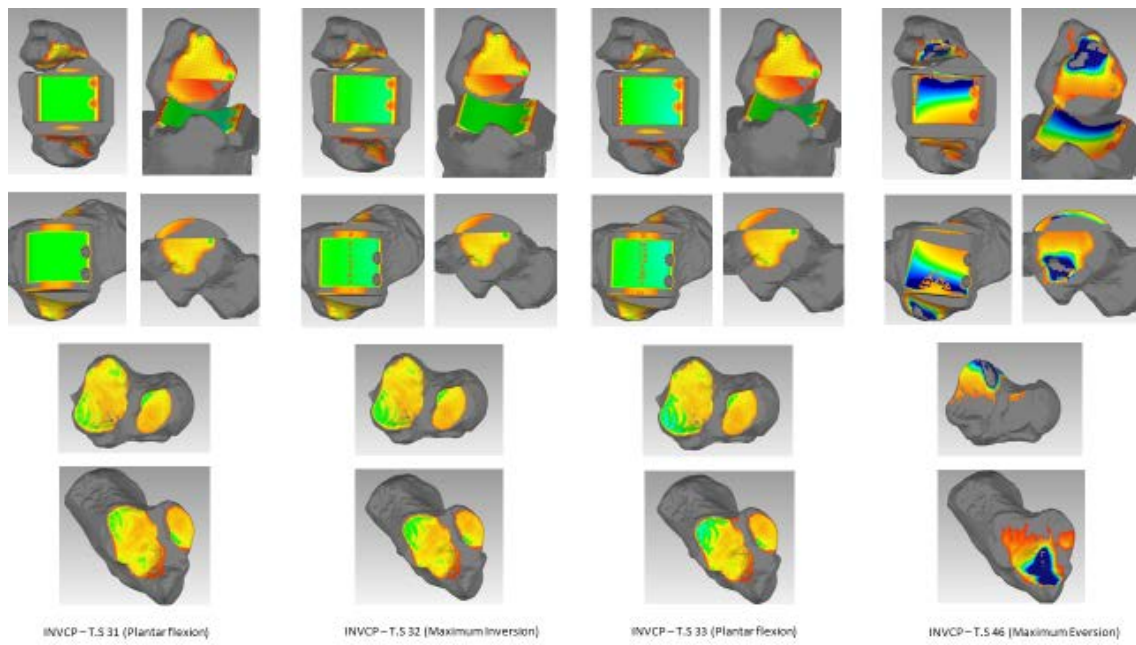
Figure 39 - INVCP - Inversion/Eversion Cylindrical Plantarflexion

DPIN – T.S 34 (Neutral position)   DPIN – T.S 40 (Maximum Dorsi flexion)   DPIN – T.S 47 (Neutral position)   DPIN – T.S 58 (Maximum Plantar flexion)
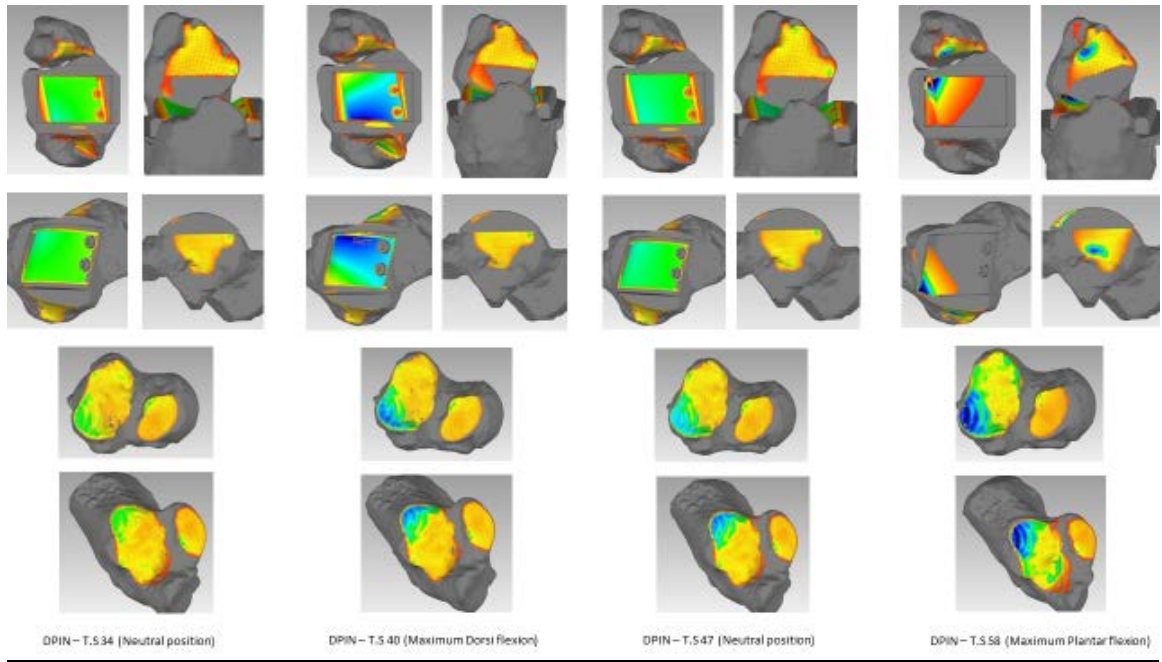
Figure 40 - DPIN - Dorsiflexion/Plantarflexion Inman Neutral

INTID – T.S 45 (Dorsi flexion)   INTID – T.S 59 (Maximum Internal Rotation)   INTID – T.S 67 (Dorsi flexion)   INTID – T.S 74 (Maximum External Rotation)
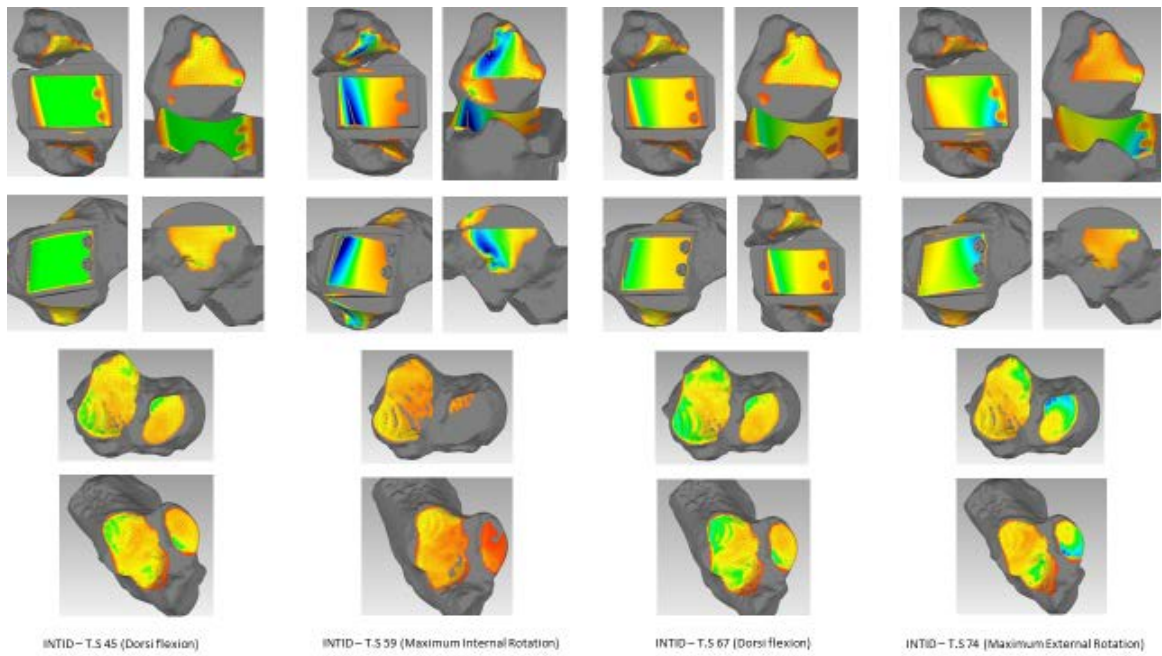
Figure 41 - INTID - Internal rotation/External rotation Inman Dorsiflexion

INTIN – T.S 49 (Neutral position)   INTIN – T.S 62 (Maximum Internal Rotation)   INTIN – T.S 71 (Neutral position)   INTIN – T.S 83 (Maximum External Rotation)
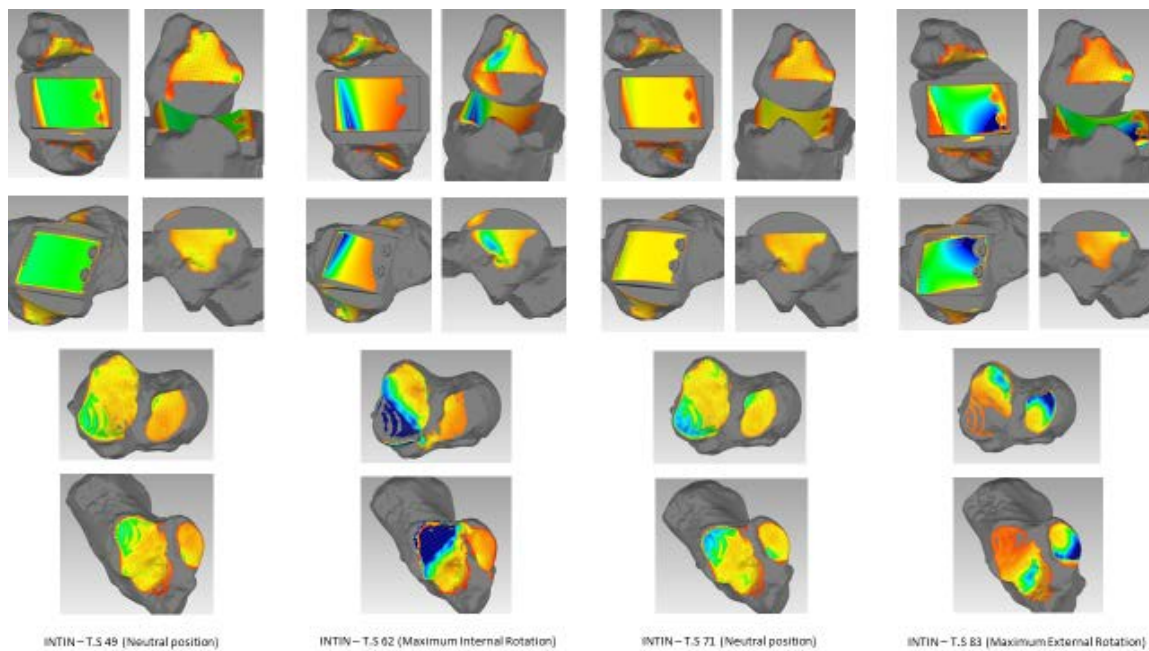
Figure 42 - INTIN - Internal rotation/External rotation Inman Neutral

INTIP – T.S 45 (Plantar flexion)   INTIP – T.S 59 (Maximum Internal Rotation)   INTIP – T.S 67 (Plantar flexion)   INTIP – T.S 74 (Maximum External Rotation)
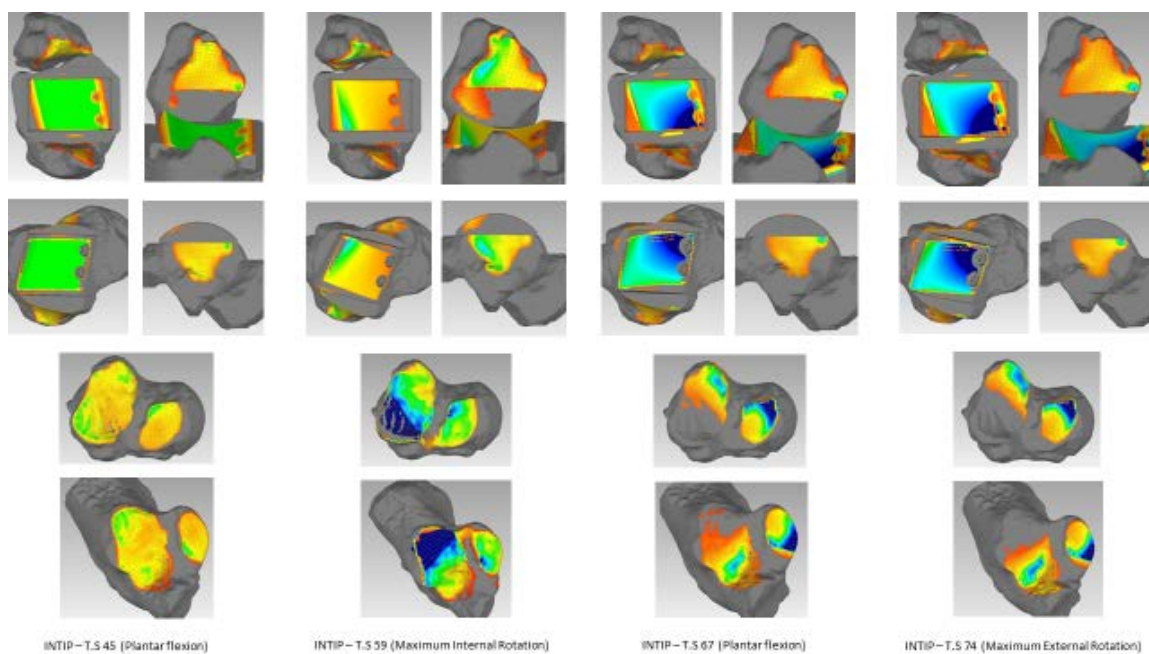
Figure 43 - INTIP - Internal rotation/External rotation Inman Plantarflexion

INVID – T.S 27 (Dorsi flexion)   INVID – T.S 34 (Maximum Inversion)   INVID – T.S 40 (Dorsi flexion)   INVID – T.S 47 (Maximum Eversion)
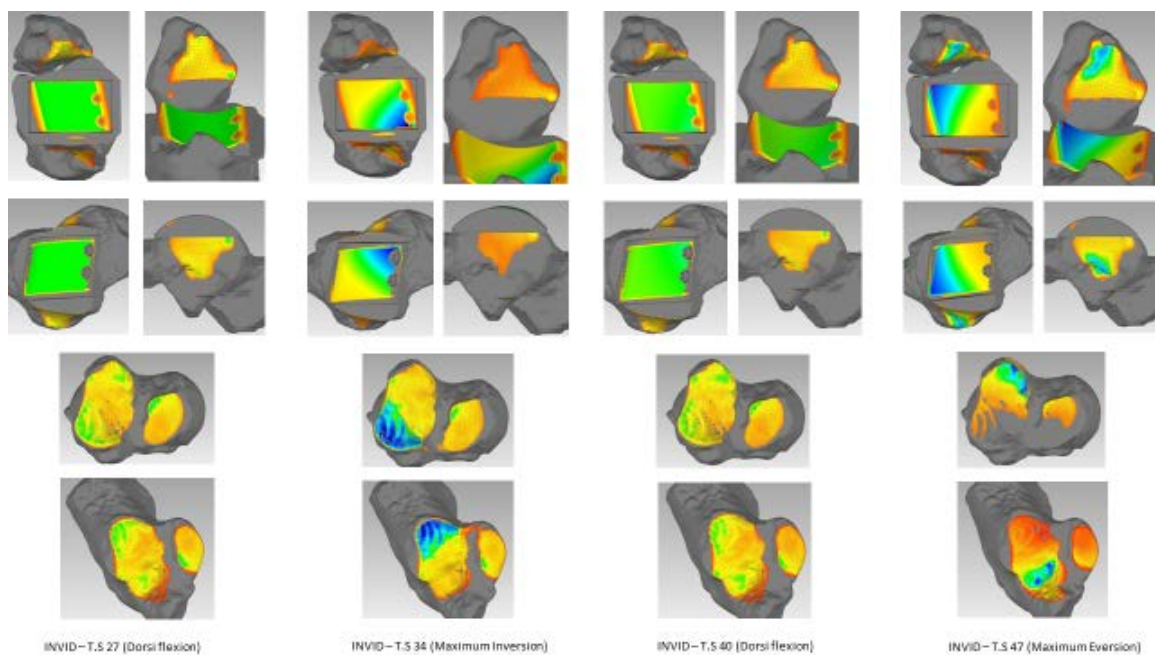
Figure 44 - INVID - Inversion/Eversion Inman Dorsiflexion

INVIN – T.S 33 (Neutral position)   INVIN – T.S42 (Maximum Inversion)   INVIN – T.S 47 (Neutral position)   INVIN – T.S55 (Maximum Eversion)
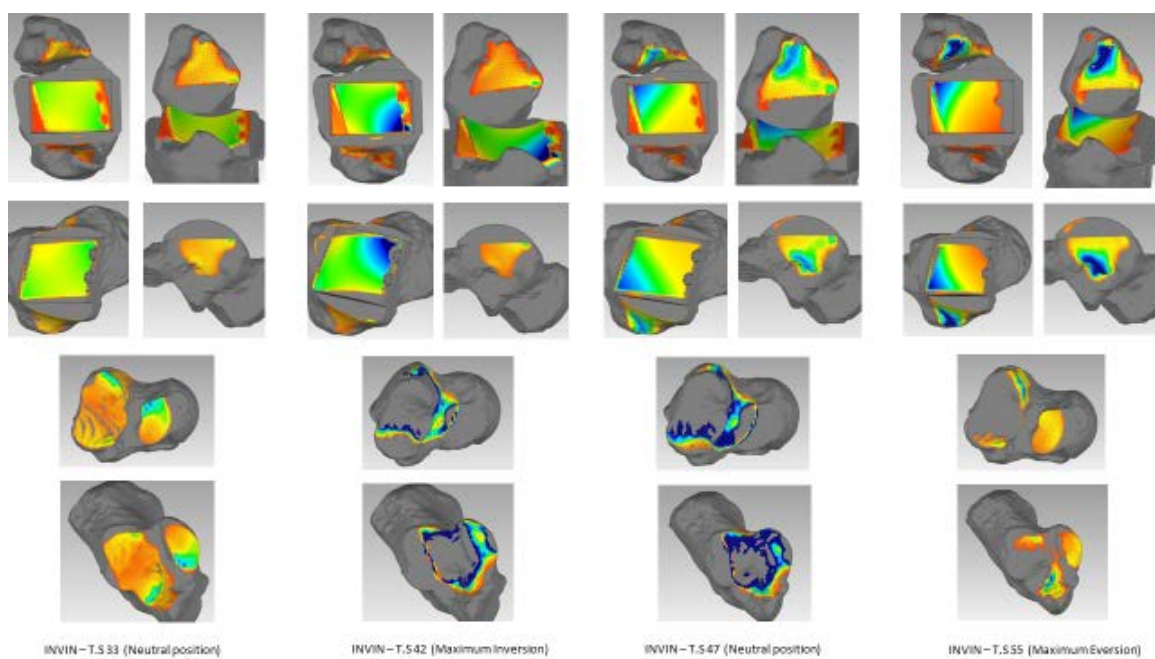
Figure 45 - INVIN - Inversion/Eversion Inman Neutral

INVIP – T.S 27 (Plantar flexion)   INVIP – T.S 34 (Maximum Inversion)   INVIP – T.S 40 (Plantar flexion)   INVIP – T.S 47 (Maximum eversion)
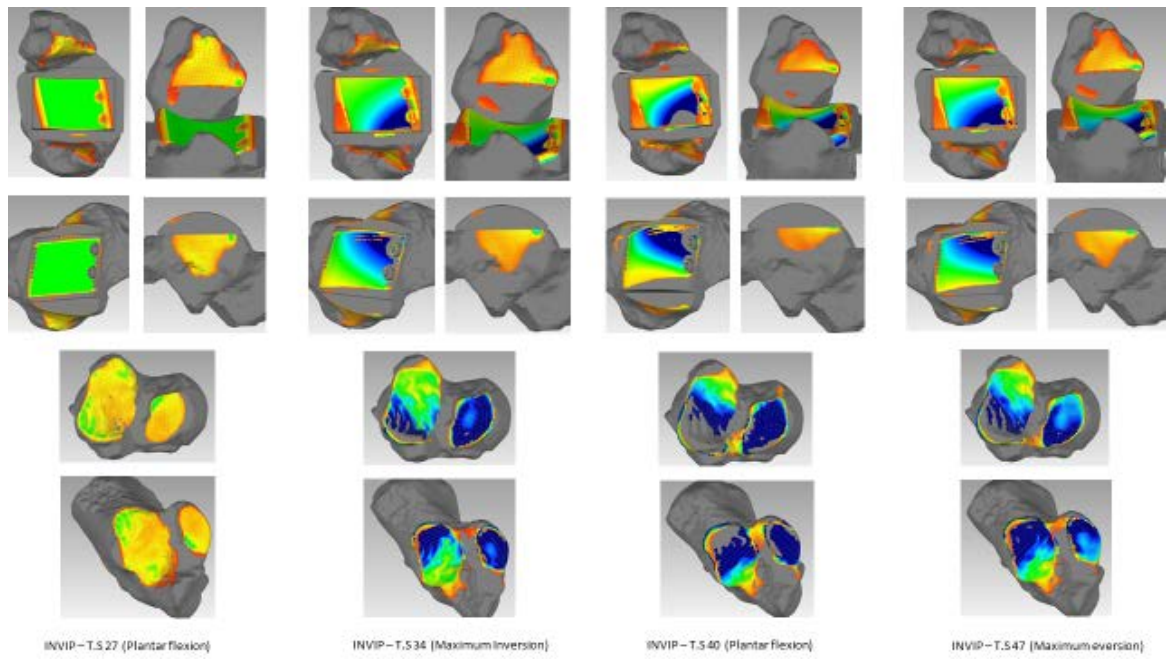
Figure 46 - INVIP - Inversion/Eversion Inman Plantarflexion

DPSN – T.S 49 (Neutral position)   DPSN – T.S 57 (Maximum Dorsi flexion)   DPSN – T.S 65 (Neutral position)   DPSN – T.S 79 (Maximum Plantar flexion)
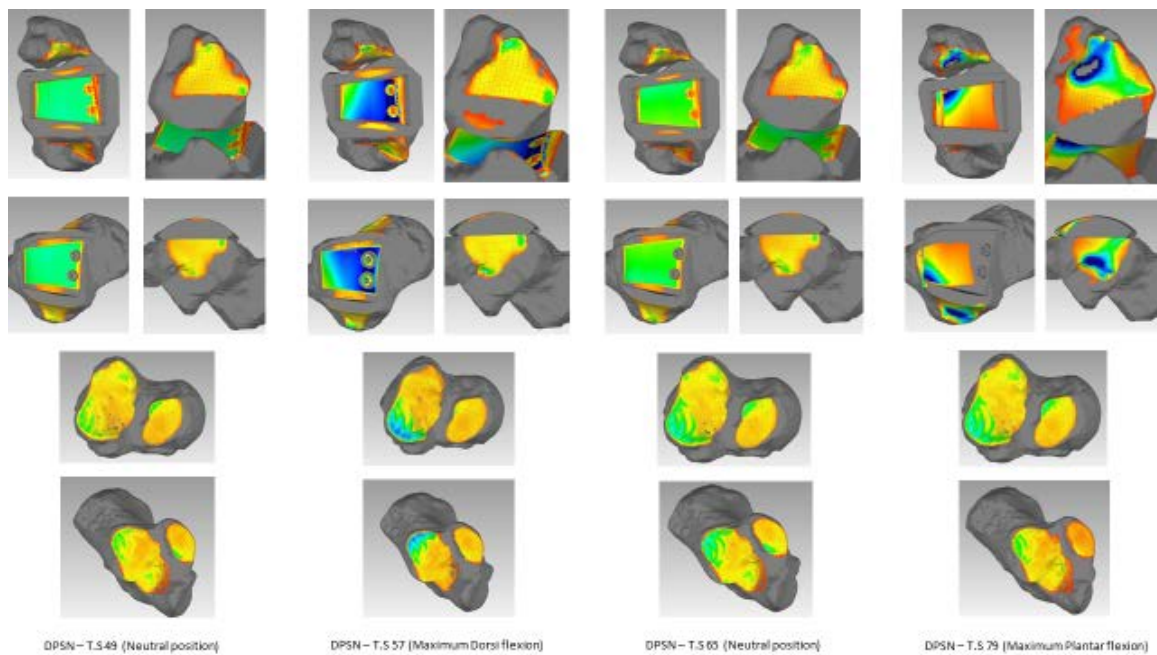
Figure 47 - DPSN - Dorsiflexion/Plantarflexion SSCL Neutral

INTSD – T.S 40 (Dorsi flexion)   INTSD – T.S 50 (Maximum Internal Rotation)   INTSD – T.S 53 (Dorsi flexion)   INTSD – T.S 67 (Maximum External Rotation)
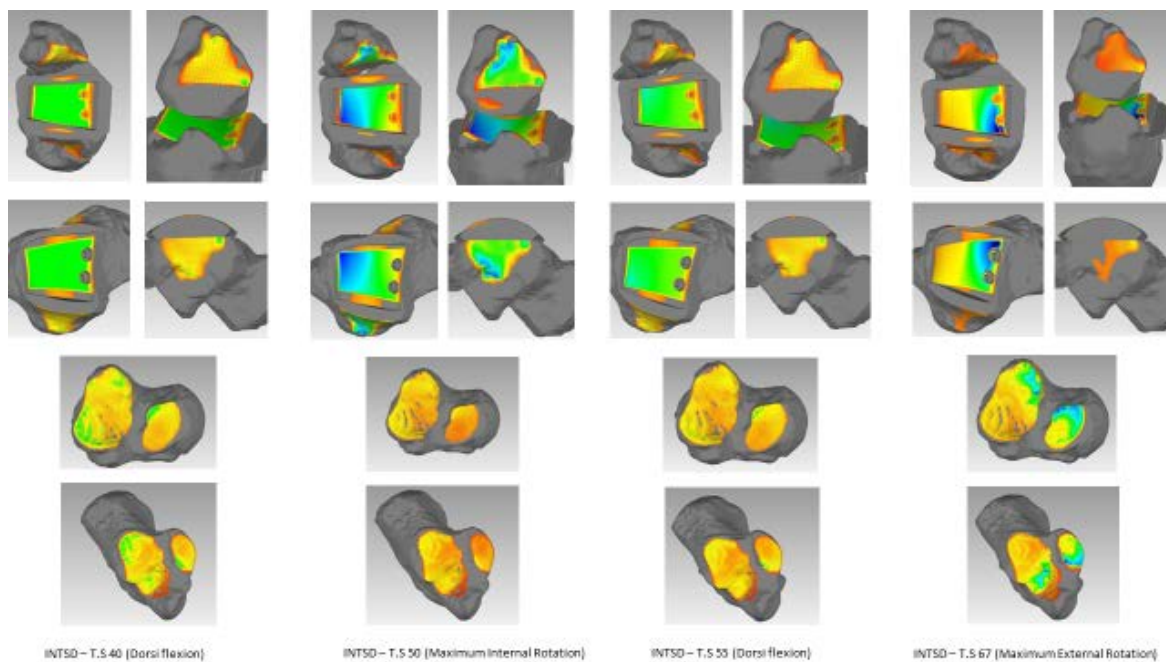
Figure 48 - INTSD - Internal rotation/External rotation SSCL Dorsiflexion

INTSN – T.S 48 (Neutral position)　　　INTSN – T.S 62 (Maximum Internal Rotation)　　　INTSN – T.S 71 (Neutral position)　　　INTSN – T.S 88 (Maximum External Rotation)
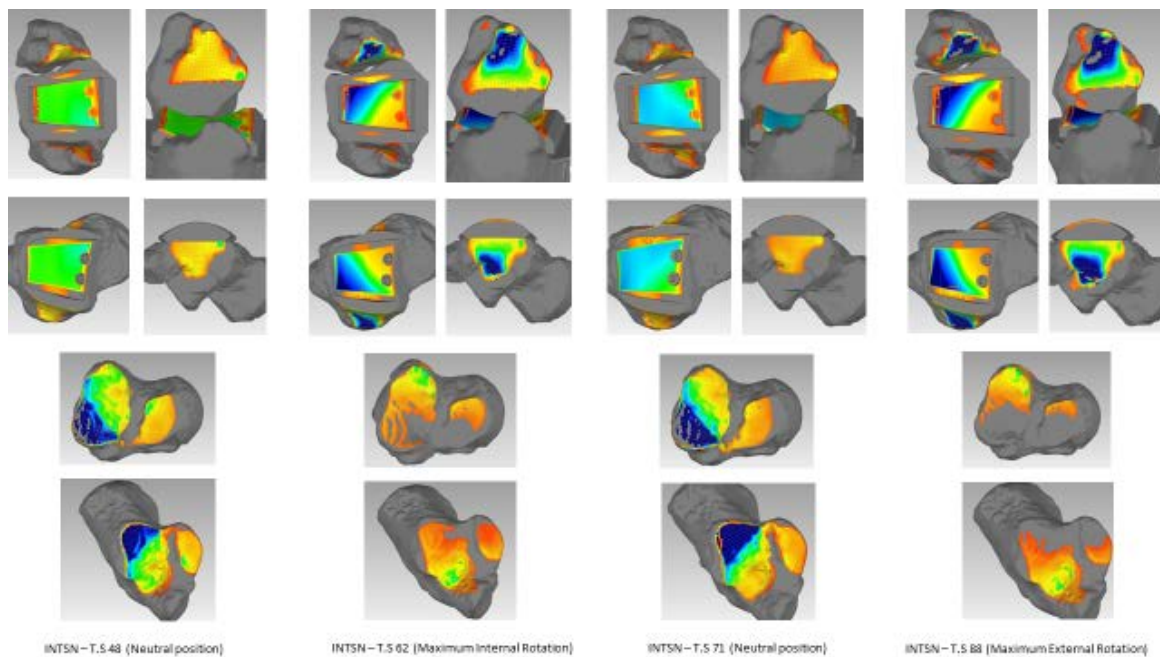
Figure 49 - INTSN - Internal rotation/External rotation SSCL Neutral

INTSP – T.S 44 (Plantar flexion)　　　INTSP – T.S 65 (Maximum Internal Rotation)　　　INTSP – T.S 65 (Plantar flexion)　　　INTSP – T.S 77 (Maximum External Rotation)
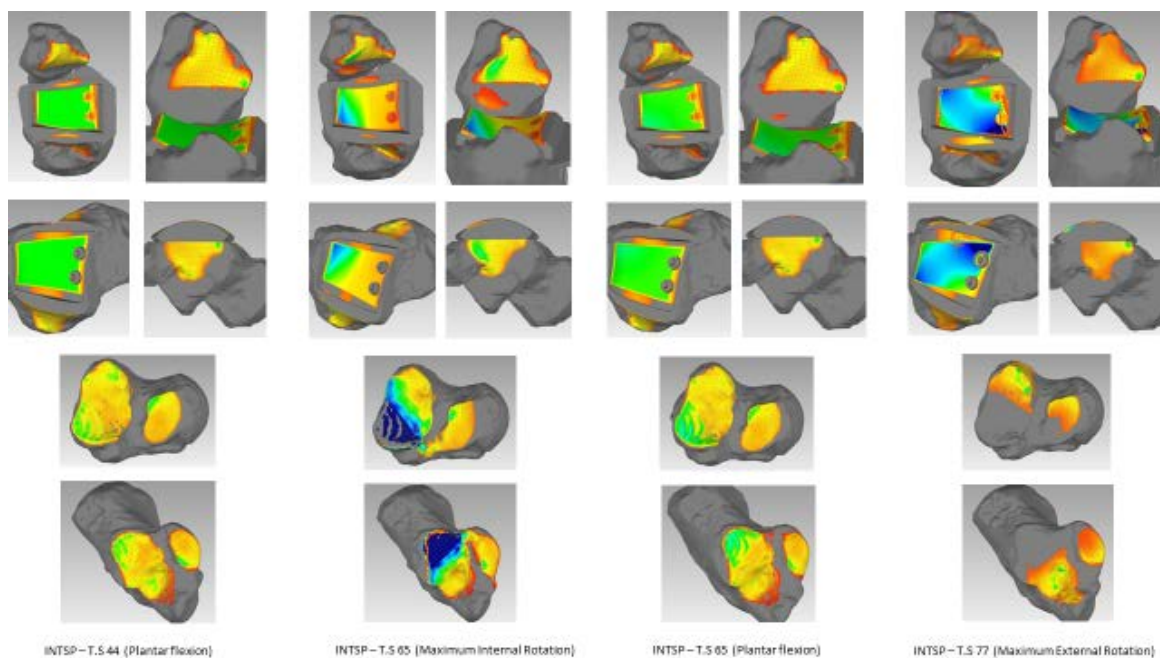
Figure 50 - INTSP - Internal rotation/External rotation SSCL Plantarflexion

INVSD – T.S 30 (Dorsi flexion)   INVSD – T.S 38 (Maximum Inversion)   INVSD – T.S 45 (Dorsi flexion)   INVSD – T.S 52 (Maximum Eversion)
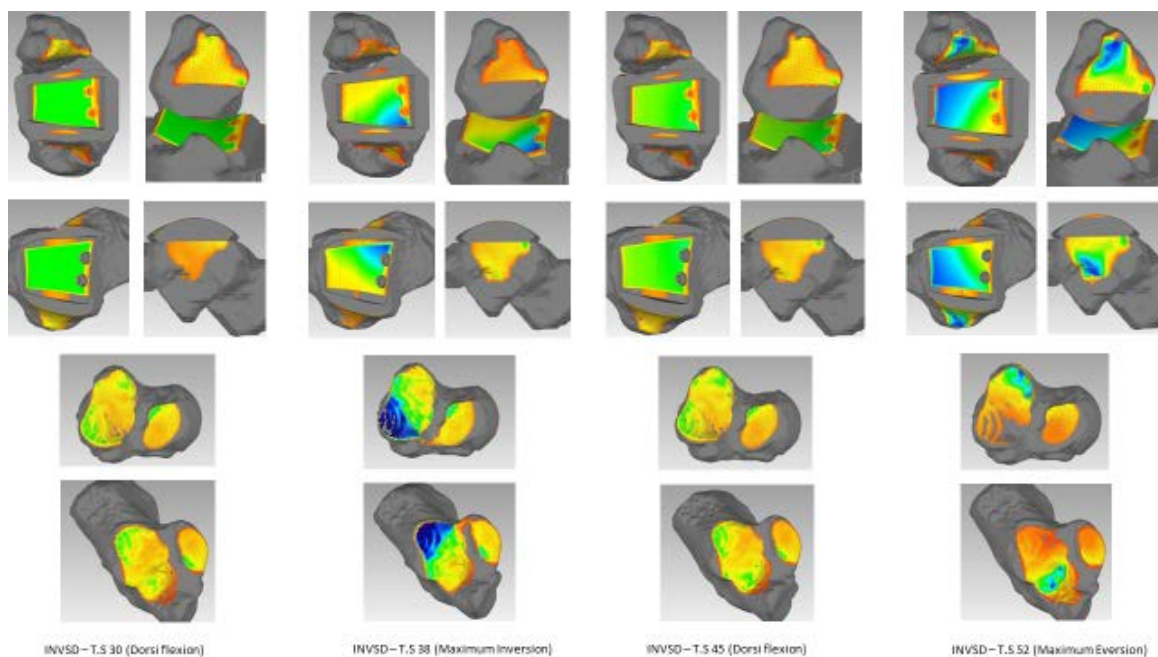
Figure 51 - INVSD - Inversion/Eversion SSCL Dorsiflexion

INVSN – T.S 36 (Neutral position)   INVSN – T.S 44 (Maximum Inversion)   INVSN – T.S 50 (Neutral position)   INVSN – T.S 58 (Maximum Eversion)
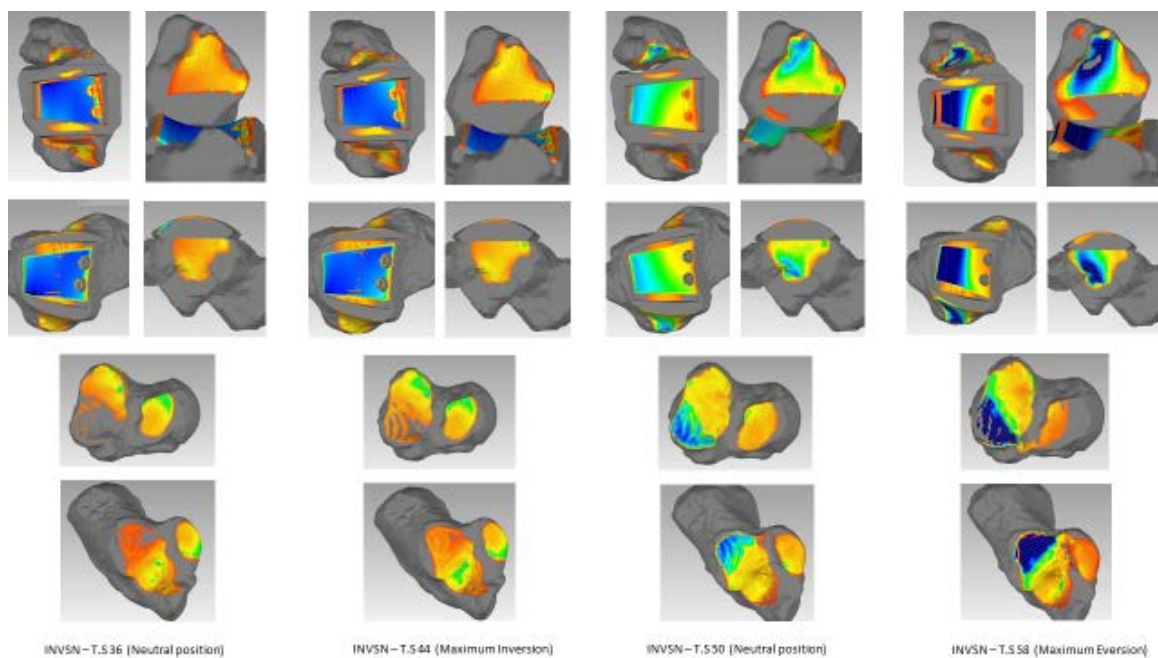
Figure 52 - INVSN - Inversion/Eversion SSCL Neutral

INVSP – T.S 34 (Plantarflexion)   INVSP – T.S 43 (Maximum Inversion)   INVSP – T.S 52 (Plantarflexion)   INVSP – T.S 60 (Maximum Eversion)

Figure 53 - INVSP - Inversion/Eversion SSCL Plantarflexion

CHAPTER 5: DISCUSSION

Distance mapping as a technique is insightful due to the nature of parameters it takes into consideration. it allows the observer to record the behavior of the articulating joints as articulating surfaces, which move together through every time step of a pre-defined motion. Apart from being able to control the angular variation between the surfaces, and the type of deviation recorded, this method essentially provides information about the motion of the articulating surfaces with respect to each other at every point of time. The use of virtual alignments in a computer software help replicate the consistency of the real-time motion of the joint (from the experimental set up) as a whole, and enable the observation of the effects of varying torque and motion type, at different time intervals on the surface geometries, in the form of displacement. The designing and modeling of different surface geometries of the articulating bones of the talocrural joint enabled the testing of this technique in varying situations.

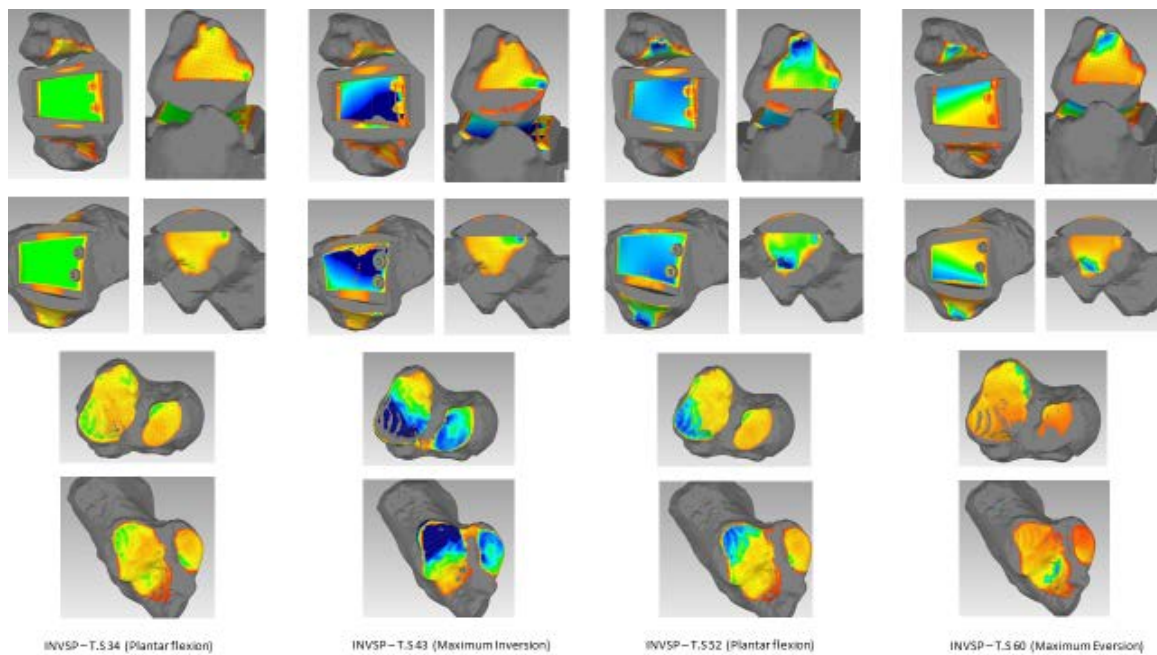The study was primarily performed to develop a technique for the surface-to-surface displacement analysis of the bones, in order to illustrate the importance of distance mapping in the evaluation of a TAR. Since the study was performed on only one specimen acting as a preliminary, it does not represent a generalization of observations for all kinds of anatomical specimens, but rather, a methodology that can be applied to evaluate the ankle bones fitted with any kind of implant, or for other joints in the body as well.

From the visuals obtained, a few noteworthy observations can be made about the relation between the type of implant (surface geometry) and the type of motion. For the motion of internal rotation/external rotation and inversion/eversion which started from initial dorsi flexion, the results of the distance mapping for almost all three implants maintained a level of consistency with respect to the amount of movement of the talus. Due to the anterior side of the tibia acting as a so-called barrier, the posterior part of the talus displayed significant contact, with the tibial plateau, which can be seen almost as a penetration. In contrast, for the internal rotation/external rotation and inversion/eversion which started

from initial plantar flexion, the distance maps were more varied from the neutral positions to either

extremity, and displayed the least deviation (most penetration) into the tibial plateau, on the medial side

of the talus. Similarities in internal rotation/external rotation and inversion/eversion starting from initial

plantar flexion were also observed for the Inman and Cylindrical implants, wherein, the talocrural joint

displayed minimal or equal change in deviation pattern over the articulating surfaces, in comparison to

the subtalar joint.

The behavior of the Inman implant during inversion/eversion starting from both dorsi flexion as well as

plantar flexion can be described as unique. During the INVID motion, there was an almost equal amount

of deviation observed in the talocrural and the subtalar joint (as mentioned earlier). This deviation was on

the anterior-medial side of the talus for maximum inversion, and on the posterior-lateral side of the talus

during maximum eversion. However, during the INVIP motion, the amount of penetration of the talus into

the tibial plateau was nearly the same as that during maximum eversion.

Similarly, for the Cylindrical implant, the INTCN case displayed minimal action in the talocrural joint, and

whatever change in deviation was observed in this joint, was pertaining to the amount of penetration

observed on the medial and lateral sides of the talus during internal rotation and external rotation

respectively. In the case of INVCD and INVCP, the posterior side of the talus digging into the tibia, was the

seen to be the most during maximum eversion, and some of the load was also seen transferred to the

subtalar joint.

In comparison to the Inman and Cylindrical implants, the behavior of the SSCL implant was strikingly

different. As opposed to the stark differences and sharply demarcated zones of deviation with the Inman

and Cylindrical surface geometries, the SSCL implant surfaces displayed a highly congruous deviation

pattern during each of the motion combinations that the cadaveric specimen was subjected to. There was

a good amount of consistency observed as far as the usage of the talar saddle was concerned, and the

transfer of motion between the medial and lateral sides of the talus was evident through the clean shift in displacement pattern over the articulating surfaces.

From the observations made for each of the implant types, in comparison to the natural, implant-less ankle, it can be duly stated that the geometry of the Cylindrical and Inman implants prevent them from being able to perform a uniform load transfer for all the different motion combinations. Both these implants have a single degree of freedom, whether it is the cylindrical surface in itself, or the conical surface that the Inman implant is a part of. In contrast, the geometry of the SSCL implant surfaces is able to provide two degrees of freedom owing to the curvatures of the saddle, thus performing better under applied torque and at varying time intervals, producing an almost even deviation between the articulating surfaces.

CHAPTER 6: CONCLUSION

From the results of this study, it can be concluded that the use of distance mapping as a tool in evaluating ankle kinematics is rather important and quite insightful. It provides a method by which any two articulating bone surfaces can be observed together for their motion, solely with respect to one another, as they move as a single unit under applied forces, through multiple time intervals. Displacement analysis can also be applied to a more complex anatomical set up, such as the interaction between one bone surface and the corresponding layer of cartilage, or under the constraint of the ligaments. It supports the idea that the morphological features of the bones, or the implant surfaces, have a definitive effect on the kinematic behavior of the ankle, as can be seen from the comparisons drawn for the three implant cases. Finally, it provides a good measuring methodology to display how any new implant surface design behaves, how the surface-to-surface motion is affected due to implant wear, and how much design modification is required to best replicate the anatomy and trends of surface contact of the natural ankle throughout the various ranges of motion.

BIBLIOGRAPHY

[1]   D. Joshua Mayich, M., MD1, Alison Novak, MSc, PhD2, Daniel Vena, MSc2, and M. Timothy R. Daniels, and James W. Brodsky, MD4, *Gait Analysis in Orthopedic Foot and Ankle Surgery—Topical Review, Part 1: Principles and Uses of Gait Analysis.* Foot & Ankle International · November 2013, 2013.

[2]   Alexander Rabinovich, M., M. Fabian Pollo, and M. James W. Brodsky, *Durability of Improvements in Gait Analysis after Total Ankle Arthroplasty.*

[3]   Keiji Iwamoto, K.S., Tetsuya Tomita, Jun Hashimoto, Takaharu Yamazaki, Hideki Yoshikawa & Kazuomi Sugamoto, *In vivo kinematics of three-component mobile-bearing total ankle replacement in rheumatoid ankle with talocalcaneal arthrodesis and spontaneous talocalcaneal fusion.* Modern Rheumatology 2014. **24**(6).

[4]   Victor Valderrabano, M.D., et al., *Kinematic Changes After Fusion and Total Replacement of the Ankle Part 3: Talar Movement.* Foot & Ankle International · November 2013, 2003. **24**(12).

[5]   Institute, S.C.O., *Anatomy of the Ankle.*

[6]   A. Leardini, J.J.O.C., F. Catani, S. Martelli, S. Giannini, *The kinematics of the ankle in the sagittal plane.* Journal of Biomechanics, 1998. **31**(1).

[7]   Siegler, S., J. Chen, and C.D. Schneck, *The three-dimensional kinematics and flexibility characteristics of the human ankle and subtalar joints--Part I: Kinematics.* J Biomech Eng, 1988. **110**(4): p. 364-73.

[8]   Leardini, A., J.J. O'Connor, and S. Giannini, *Biomechanics of the natural, arthritic, and replaced human ankle joint.* J Foot Ankle Res, 2014. **7**(1): p. 8.

[9]   Lundberg, A., *Kinematics of the ankle and foot. In vivo roentgen stereophotogrammetry.* Acta Orthop Scand Suppl, 1989. **233**: p. 1-24.

[10] Lundberg, A., et al., *The axis of rotation of the ankle joint.* J Bone Joint Surg Br, 1989. **71**(1): p. 94-9.

[11] Foumani, M., et al., *In-vivo three-dimensional carpal bone kinematics during flexion-extension and radio-ulnar deviation of the wrist: Dynamic motion versus step-wise static wrist positions.* J Biomech, 2009. **42**(16): p. 2664-71.

[12] Siegler, S., et al., *The Clinical Biomechanics Award 2013 -- presented by the International Society of Biomechanics: new observations on the morphology of the talar dome and its relationship to ankle kinematics.* Clin Biomech (Bristol, Avon), 2014. **29**(1): p. 1-6.

[13] Siegler, S., et al., *Mechanics of the ankle and subtalar joints revealed through a 3D quasi-static stress MRI technique.* J Biomech, 2005. **38**(3): p. 567-78.

[14]   Mankarious, W.G., *Three dimensional kinematic and surface interaction analysis of a novel total ankle replacement surface design using a numerical model of the hind foot.* 2014.

[15]   Siegler, S., et al., *A six-degrees-of-freedom instrumented linkage for measuring the flexibility characteristics of the ankle joint complex.* J Biomech, 1996. **29**(7): p. 943-7.

[16]   S. Siegler, C.B., A. Ensini, P. Caravaggi, R. Namani, S. Durante, A. Leardini, *Effect of variation in ankle morphology on replaced joint kinematics and load transfer.* Foot and Ankle Surgery, 2016. **22**(2, Supplement 1): p. 2.

[17]   Cappozzo, A., et al., *Position and orientation in space of bones during movement: anatomical frame definition and determination.* Clin Biomech (Bristol, Avon), 1995. **10**(4): p. 171-178.

[18]   Grood, E.S. and W.J. Suntay, *A joint coordinate system for the clinical description of three-dimensional motions: application to the knee.* J Biomech Eng, 1983. **105**(2): p. 136-44.

[19]   Control™, G., *Geomagic Control™ Help Guide - 3D Deviation.* 2014.